Axonal Transport: How High Microtubule Density Can Compensate for Boundary Effects in Small-Caliber Axons

Juliana C. Wortman,[†] Uttam M. Shrestha,[†] Devin M. Barry,[‡] Michael L. Garcia,[§] Steven P. Gross,[†¶] and Clare C. Yu[†*]

[†]Department of Physics and Astronomy, University of California, Irvine, Irvine, CA 92697; [‡]Center for the Study of Itch, Washington University School of Medicine, St. Louis, MO 63110; [§]Biological Sciences, University of Missouri, Columbia, MO 65211; and [¶]Department of Developmental and Cell Biology, University of California, Irvine, Irvine, CA 92697

ABSTRACT Long-distance intracellular axonal transport is predominantly microtubule-based, and its impairment is linked to neurodegeneration. In this study, we present theoretical arguments that suggest that near the axon boundaries (walls), the effective viscosity can become large enough to impede cargo transport in small (but not large) caliber axons. Our theoretical analysis suggests that this opposition to motion increases rapidly as the cargo approaches the wall. We find that having parallel microtubules close enough together to enable a cargo to simultaneously engage motors on more than one microtubule dramatically enhances motor activity, and thus minimizes the effects of any opposition to transport. Even if microtubules are randomly placed in axons, we find that the higher density of microtubules found in small-caliber axons increases the probability of having parallel microtubules close enough that they can be used simultaneously by motors on a cargo. The boundary effect is not a factor in transport in large-caliber axons where the microtubule density is lower.

INTRODUCTION

Long-distance vesicular transport is critical for axonal function, and its failure may induce neurodegeneration (1,2). However, exactly what factors contribute to its robustness or failure is still not well understood. Much of the transport occurs along microtubules (MTs). Electron micrographs indicate that the packing density of MTs in axons increases as the axon caliber decreases, ranging from ~ 150 MTs/μm^2 of cross-sectional area of axoplasm for small unmyelinated axons (which are less than 1 μm in diameter), to less than 15 MTs/μm^2 in the axoplasm of large myelinated fibers of ~ 10 μm in diameter (3–6). In this study, we propose that the higher density of MTs found in small-caliber axons can compensate for confinement effects that can impede axonal transport in axons with a narrow diameter.

To date, it has been implicitly assumed that transport in axons is essentially the same as transport in the neuronal cell body. However, the previously unexplored effect of boundary conditions may make transport in these two areas quite different. In this paper, we propose that the long cylindrical geometry of the axon—with the close presence of the axonal membrane—leads to two classes of effects, both of which impair transport. These are 1), a wall effect (reflecting a "no-slip" boundary condition) in small-caliber axons and 2), an enhancement of macromolecular crowding.

The wall effect results from simple hydrodynamics: as a cargo moves along an MT in a small-caliber axon as shown in Fig. 1 *A*, it experiences a larger viscous drag than it would if it were moving in the cell body far from the cell walls. This is because of the no-slip or low-slip boundary condition of the cytosol at the axonal wall and also at the surface of the cargo, so that the closer the cargo is to the wall, the more shear there is, the larger the effective viscosity is, and the larger the opposition to motion. (The no-slip boundary condition refers to the fact that the fluid next to a surface cannot move or flow.) The second effect is an enhancement of the opposition to motion because of crowding, and conceptually results from an inability of large molecules to move out of the way of the cargo as it moves down the axon; as large molecules try to move away from the oncoming cargo, their motion is impeded by the presence of the nearby walls or boundaries. To illustrate these effects, we have used a simple model. We find that by walking along parallel MTs (see Fig. 1 *A*), multiple motors can be employed to dramatically improve transport by overcoming such opposition to motion.

Using a three-dimensional (3D) Monte Carlo simulation to model vesicular transport in an axon, we find that the single motor run length is significantly reduced because of the boundary or wall effect. This dramatic effect on axonal transport has not been considered before. We propose that axonal transport uses multiple motors moving along more than one MT to overcome this impediment (see bottom of Fig. 1 *A*). In particular, we suggest that the high density of MTs in small-caliber axons ensures that there will be a high probability of closely spaced parallel MTs that can promote multiple-motor-based transport along more than one MT, dramatically improving transport of cargos with multiple motors.

Submitted November 4, 2013, and accepted for publication December 31, 2013.

*Correspondence: cyu@uci.edu

Juliana C. Wortman and Uttam M. Shrestha contributed equally to this work.

Steven P. Gross and Clare C. Yu are co-senior authors.

Editor: Edward Stuenkel

0006-3495/14/02/0813/11 $2.00

http://dx.doi.org/10.1016/j.bpj.2013.12.047

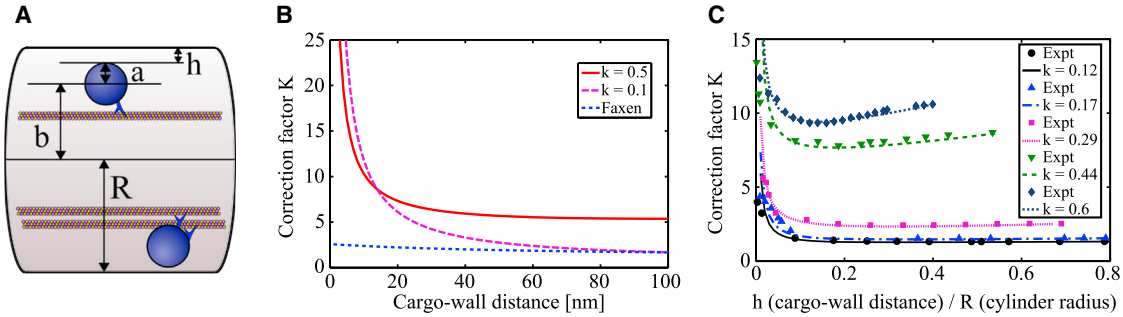

FIGURE 1 (*A*) Cargos being hauled by motors along MTs inside an axon. The spherical cargo has a radius a in a cylindrical axon of radius R. The center of the cargo is displaced a distance b from the axon's axis. The distance h is the closest approach of the cargo to the axon wall. Two scenarios are shown. The top shows a single motor hauling a cargo along an MT. The key point of this paper is that the enhanced viscosity encountered by the cargo near the wall of the axon can be overcome by having multiple motors hauling the cargo along closely spaced parallel microtubules as shown at the bottom. (*B*) Correction factor K from Eq. 2 for a sphere of radius 250 nm for two axon diameters ($k = 0.1$ and $k = 0.5$) as a function of the cargo-wall distance h. As a comparison, we have also shown the correction factor obtained from the Faxén formula (*blue dotted line*) for the same parameters. Far away from the wall in a large axon (*magenta dashed curve*) our theory agrees well with Faxén's law. Note that for a relatively large cargo (250 nm radius) in a relatively small axon ($k = 0.5$, corresponding to a 1 μm diameter axon, *solid line*), the "edge" effect, represented by the correction factor, extends over the width of the axon, even when the cargo is far away from the wall. (*C*) Comparison of the theoretical correction factor K given by Eq. 2 to experimental data (82) for a sphere moving through a fluid-filled cylinder for various values of $k = a/R$. To see this figure in color, go online.

Our paper is organized as follows. We begin by showing that a sphere (cargo) moving through a fluid filled cylinder (axon) can experience significant drag if it is close to the wall of the cylinder. After describing our simulation procedure, we show that this viscous drag can reduce the run length of a cargo being hauled by a single motor along an MT in a cylinder, and describe how this effective viscosity in the fluid-filled cylinder can be further enhanced by macromolecules. We then show that a way to overcome this opposition to cargo transport is to use multiple motors to haul the cargo along two parallel MTs (see bottom of Fig. 1 *A*); if the MTs are close enough, because each motor's "on" rate is effectively doubled, the presence of the second MT dramatically enhances the number of engaged motors. Thus, the high density of MTs found in small-caliber axons can help to compensate for the confinement effects of viscous drag on axonal transport. Interestingly, boundary effects should not impede cargo transport in large-caliber axons where there is a much lower MT density.

Heuristic approach: Wall correction increases as the cargo approaches the wall

Generally, the viscosity of axoplasm or cytosol depends on the length scale at which it is measured. For example, substances squeezed from nerves and assumed to be axoplasm were reported to have a viscosity 10^6 times greater than that of water (7), though this can be attributable to the cross-linking and frictional interactions between neurofilaments and MTs in the axoplasm (8). On the other hand, electron spin resonance measurements of the microviscosity of mammalian nerve axoplasm found a value ~ 5 times larger than the viscosity of water (9). This viscosity is not enough to seriously oppose motion, at least not in *Drosophila* embryos (10).

We considered the possibility that in the axon, the *effective* viscosity might be enhanced by the presence of the wall, attributable to both a direct effect of no-slip boundary conditions as well as the effect of the wall on the mobility of large macromolecules in the axoplasm. We first investigated the potential importance of a no-slip boundary condition. We considered a spherical cargo of radius a moving in a cylindrical axon of radius R (Fig. 1 *A*), with η_∞ the viscosity of the axoplasm in an unbounded medium. The Stokes force experienced by the cargo moving with velocity $\boldsymbol{v}$ in the laboratory frame of reference can be expressed as (11) follows:

$$\boldsymbol{F} = 6\pi\eta_\infty a\boldsymbol{v}K, \tag{1}$$

where K (>1) is the correction factor because of the wall effect. We assume a cargo velocity parallel to the axon axis; K depends on the position (relative to the axon wall) and radius of the cargo, as well as the axon diameter (2R).

The exact solution for K for a sphere moving on the axis of a cylinder filled with viscous fluid has been obtained numerically by solving a set of linear equations (11,12). Further, some special solutions can be found perturbatively when the sphere is near the axis of the cylinder (13–15). However, there is no general solution that applies over the entire range of positions and sizes of the sphere. Here, by exploiting the approximate behavior of the solutions near the axis and near the wall, we can write an approximate overall solution as a superposition of these solutions (Eq. 2), which is valid over a suitable range of the parameters (see the Supporting Material):

$$K = \exp(-k\varepsilon)\ K_0 + k^2\varepsilon^2\ f(\varepsilon)(R/h) \tag{2}$$

This approximate solution is written in terms of the eccentricity parameter $\varepsilon = b/R$ and the dimensionless radius of the sphere $k = a/R$, where b is the distance of the center of the sphere from the axis of the cylinder and R is the radius

of the cylinder. Here, K_0 is the wall correction factor for rigid spheres moving in a still liquid along the axis of a cylindrical tube ($b = 0$) (11), and $f(\varepsilon)$ is the Brenner eccentricity function (11). We give the approximations that we used for K_0 and $f(\varepsilon)$ in the Supporting Material. H is the distance between the surface of the cargo and the inner surface of the axon. Eq. 2 recovers the previously obtained results for both limiting cases $\varepsilon \to 0$ and $h \to 0$.

In Fig. 1, we show the correction factor K as a function of the sphere-cylinder surface to surface distance h. Two general features of our results are of interest. First, relatively close to the wall, the boundary effect is very large, and second, for cargos that are relatively large with respect to the caliber of the axon (i.e., roughly filling it by half), the "wall" effect is evident even quite far away from the wall. For example, if we think of $\eta_{eff} = K\eta_\infty$ as an effective viscosity, then η_{eff} can be 50 times that of water for $K = 5$ and $\eta_\infty = 10$ times that of water (9).

METHODS

Modeling and numerical simulation

We used a previously developed 3D Monte Carlo model (16) to study the transport of cargos hauled by kinesin motor(s). Kinesin molecules were bound to a spherical cargo, and the "heads" of the motors were free to search for binding domains of the MT that were within reach. Once the head could reach the MT, we assigned a probability of the motor binding to the MT, based on an on-rate of 2 s^{-1}. We ignored head-head dynamics of a motor, and as others have done, simply modeled kinesin as a single head that hopped from one binding site to the next with step size of $d = 8$ nm, moving toward the plus end of the MT. Since modeling single-motor kinesin stepping followed previously published work, simulation details are left to the Supporting Material. However, we note that in addition to the forces acting on the cargo because of the molecular motors and viscous drag, it also underwent Brownian motion.

Cargo dynamics

In a viscous medium, a cargo hauled along an MT exhibits translational as well as rotational Brownian motion. Throughout our simulations, the motor-cargo system satisfied the following boundary conditions: 1) the motor(s) could not go into the cargo or the MT; 2) the cargo could not go into the MT; 3) the cargo had to be inside of the axon. Unless explicitly stated, the cargo radius was $a = 250$ nm whereas the MT radius was $r = 12.5$ nm. The coefficient of viscosity of the axoplasm was assumed to be 10 times that of water (9). All the physical properties were averaged over 1000 realizations. To avoid possible divergences in the numerical simulations, we introduced a 1 nm artificial clearance between the cargo-wall surfaces.

Modeling macromolecules in the axoplasm

To investigate theoretically how large macromolecules could hinder cargo transport through the cytoplasm and axoplasm, we included polymers in our simulations of a cargo moving in a fluid-filled axon. The study of the detailed molecular structure and dynamics of long chain molecules using a microscopic model such as a "molecular dynamics" approach is computationally challenging. To simplify this, we modeled each polymer as a chain of beads, coupled through massless springs. Each bead performed constrained diffusive motion and interacted with the cargo and with the beads of nearby chains. We assumed that the interactions could be approximated by a Lennard-Jones (LJ) type potential to take into account both the long-range attractive and short-range repulsive forces. The details of the model and calculations are given in the Supporting Material.

To quantify the effect of macromolecule-cargo interactions, we considered a spherical cargo being dragged through a cylindrical tube by an external force F through a fluid with polymers (see Fig. S3 *A* in the Supporting Material), i.e., the cargo was not being hauled by molecular motors. We calculated the (size-dependent) effective viscosity to which the cargo was subjected as follows:

$$\eta_{eff} = \frac{F}{6\pi a v} = K\eta_\infty, \tag{3}$$

where F was the external driving force and v was the average velocity of the cargo. We solved the Langevin equation for the motion of a cargo driven by the external force (see Fig. S3 *A*). We randomly distributed the polymers in a tube of a given diameter and initially placed the cargo on the axis. The cargo interacted with each bead of the polymer as well as experienced the drag force because of proximity to the wall of the tube. The polymer-polymer interactions were also incorporated through bead-bead interactions. In this way, we measured the approximate time for a given fixed-travel distance along the axis and calculated the average velocity of the cargo.

RESULTS

Wall effect on transport by a single motor

We first explored how the wall would modify axonal transport of a cargo hauled by a single kinesin motor. We modeled the axon as a long cylinder of uniform diameter with an MT centered along the axis of the axon. (In practice, electron micrograph images (17) show a wide variation both in the caliber size and longitudinal undulation.) We investigated the magnitude of the wall effect on cargo motion via our simulations (Fig. S2), and consistent with the analytic results in Fig. 1, found that the run length decreased as the diameter of the axon decreased. For a D = 1200 nm axon with $\eta_\infty = 10$ times that of water, and with the 500 nm diameter cargo, the average load on the motor during the simulation was ~ 0.84 pN; the effect of such a load in our simulations in the presence of Brownian motion was consistent with past experimental results (18) and previous force-processivity data (18). Thus, for some parameter values, the effect of the increased drag because of the wall effect can be enough to decrease by ~ 50% the expected mean travel distance of a cargo that is hauled by a single motor. Such an effect would likely not be insignificant from a physiological point of view, since recent work (19) suggests that a roughly 25% decrease in motor processivity is enough to have significant consequences. Note that the parameters for the large cargo/small axon case considered are not unreasonable, since mitochondria are frequently on the order of 200 nm in diameter (20), and there are numerous axons on the order of 1 μm in diameter.

Potential effect of crowding

The biological medium differs from an idealized Newtonian fluid, in part because of large molecules or parts of large molecules that can impede cargo motion because of steric hindrance. For example, electron micrographs of MTs with MT-associated proteins (MAPs) bound to them have projections extending ~ 100 nm away from the surface of the MT (21,22). Neurofilaments are oriented axially, parallel to the MTs. Quick-freeze deep-etch micrographs of frog axons reveal that the C termini of neurofilaments medium and heavy have long side arms that project 20 to 50 nm laterally outward from the filament core (22–24). There is also a family of very large cytoskeletal linking proteins called plectins that have globular multiinteractive end domains separated by an α-helical sequence dimerized with another molecule to form a 190 nm-long coiled coil rod domain (25). The major isoform found in neural cells is plectin 1c (26). It is not known if there are free-floating large molecules in the axon, partly because to extract the cytoskeleton to perform the quick-freeze deep etch, which is the gold standard for determining axoplasm structure, anything that is not anchored to the cytoskeleton is washed away. If there are such large molecules in the axoplasm, their movement could be restricted because of the confined geometry, resulting in a significant enhancement of their opposition to the cargos' motion. MAPs, C termini of neurofilaments medium and heavy, plectin 1C, and other large molecules could result in increased average viscous drag, reducing the cargo's run length.

To investigate theoretically how large molecules could hinder cargo transport through such effects, we simulated a spherical cargo moving through a cylindrical axon with a polymer-filled fluid under the influence of an external force as described in the Methods section. The results are shown in Fig. S3. We found that the higher the polymer concentration, the larger the viscosity was. In Fig. S3, we separated the wall effect from the viscous effect of the polymers alone on the cargo mobility (quantified in terms of effective viscosity) for different polymer concentrations. (We can turn off the wall effect by setting the viscosity correction factor $K = 1$ in Eq. 2.) As Fig. S3 *B* shows, without the wall effect, there was a significant enhancement of the "base" viscosity of the medium as the concentration of the polymer increased. This enhancement came from the excluded volume effect. When the wall effect was included (see Fig. S3 *C*), the effective viscosity remained fairly constant for a given volume exclusion (polymer concentration) in large-diameter axons. However, the wall effect became important and was the dominant factor inhibiting cargo mobility as the caliber size decreased, and the presence of the polymers increased the wall effect. The length scales for which the wall effect became important are discussed next.

Onset of the wall effect when the cargo radius and cargo-wall distance are comparable

Noting that the presence of long molecules dramatically enhanced the opposition to the motion for even a relatively small cargo in a small-caliber axon, we wanted to better understand how the onset of huge resistance depended on the different length scales of the system. So we varied the radius of the cargo (a), the diameter of the axon caliber (D), and the length of the polymers (L), and the distance of the surface of the cargo to the inner wall of the axon (h). The details of the simulation are given in the Supporting Material. Our results are shown in Fig. 2 where we see that, irrespective of the axon or cargo size, the effective viscosity dramatically increased when $h/a \leq 1$ for all axon and cargo dimensions. Physically, small h meant that the cargo was close to the wall, and large a meant that there was a large amount of cargo surface area to enhance the viscous drag produced by proximity to the wall of the axon. Thus the wall effect became insignificant if the cargo-axon geometry satisfied the condition $h/a \gg 1$.

For a moderate size axon ($D \sim 1$ μm) and for small cargos ($a \sim 50$ nm), the enhancement of viscosity merely came from the steric hindrances because of the cargo-polymer interactions, and the wall effect, in most of these circumstances, could be comfortably ignored. On the other hand, cargos can be relatively large membranous organelles such as mitochondria and lysosomes ($a \sim 0.5$ μm). The wall effect and confinement becomes more relevant for such big cargos especially when $h/a \to 1$.

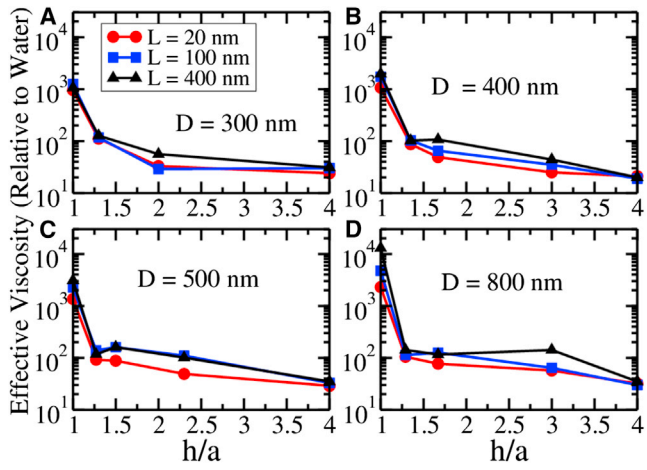

FIGURE 2 Effective viscosity of the medium in the presence of the macromolecules of length L as a function of the ratio of the cargo-cylinder surface-to-surface distance h to the radius a of the cargo. (*A*) Axon diameter $D = 300$ nm; (*B*) $D = 400$ nm; (*C*) $D = 500$ nm; and (*D*) $D = 800$ nm. Irrespective of the caliber D, there is dramatic increase in the effective viscosity when this ratio h/a is of the order of or less than one. Polymer concentration is fixed at 4.17% excluded volume. For $L = 20$, 100, and 400 nm, this excluded volume corresponds to concentrations of 16.5, 3.31, and 0.827 μM, respectively. To see this figure in color, go online.

These studies, then, suggest that the presence of the axon membrane can in some circumstances contribute to significant opposition to cargo motion, especially for large cargos; the exact amount of resistance will depend on the size of the cargo relative to the axon diameter, on the cargo position relative to the axon wall, and also on the extent of large macromolecules/polymers locally present. We note that these effects likely vary spatially and temporally; e.g., even in a relatively large axon, when two large cargos pass each other, they may push each other against the side walls, temporarily decreasing h and satisfying the condition $h/a<1$ (see also Discussion). Such effects are potentially problematic because axons rely on long-distance transport, and its impairment would seriously compromise axonal health. Since groups of molecular motors can exert more force, and provide a more robust transport system under load, one axonal strategy to move given cargos further and more robustly might be to maximize the number of engaged motors. We therefore examined whether there were any structural features that might promote such increased motor engagement.

Transport along multiple microtubules enhances overall motor on-rates

Studies from multiple groups (27,28) indicate that the more molecular motors that move a cargo, the further the cargo is expected to move and the greater the force that moves it. In vivo, multiple motors typically move a cargo (19,29,30). Although multiple factors can affect exactly how many motors are engaged at any instant, one strong contributor is the motors' on-rates, that is, how long it typically takes them to bind to the MT. The higher the average on-rate is, the more available motors there are that are engaged in hauling the cargo at any given instant (18,31).

Suppose that a single motor has an on-rate of k_{attach}^{single}, with a probability of binding in a time interval Δt equal to $k_{attach}^{single}\Delta t$. If there are N total motors, with those bound to the MT denoted by N_{bound}, then the number of free motors is $N_{free} = N - N_{bound}$. In principle, the rate at which motors on a cargo can bind to an MT, i.e., the number of motors that bind per second, is determined by the state of the cargo, i.e., not only the number of free motors, but also the number of motors already bound to the MTs that could interfere with each other. However, for the simplest case (assumed here) all the motors were clustered at a point, and the motors did not directly interact with each other, so that the effective on-rate (number of motors that bind per second) was simply proportional to the number of free motors. Thus, when $N_{free} = 1$, the on-rate is k_{attach}^{single} but if $N_{free} = 3$, for instance, the effective on-rate for any additional motor to bind is $3\ k_{attach}^{single}$, that is, three times as large. Now, in principle, if a second MT was parallel—and sufficiently close—to the first, any free motor could bind either to the first or the second MT, so that potentially, each motor had effectively twice as many chances to bind, that is, each motor's on-rate is doubled.

Intriguingly, the magnitude of the hypothetical effect of having two parallel MTs increases with the number of motors present: if we imagine $N_{free} = 1$, then when a single MT is present, the on-rate would be k_{attach}^{single}, but when two MTs are present, we might expect that the effective on-rate to be $2k_{attach}^{single}$. However, if $N_{free} = 4$, then the on-rate goes from $4\ k_{attach}^{single}$ for a single MT to $8\ k_{attach}^{single}$ for two MTs. In other words, for the one-motor case, to double the on-rate, one can either add a second motor, or add a second MT; however to achieve an on-rate 8 times that of a single motor, one can either start from the $N_{free} = 4$, and add an additional *four* motors, or simply add a *second* MT. This sort of argument suggests that clustering a few MTs close together might be a very efficient way to improve motor utilization, especially for cargos that potentially have more than two active motors. Note also that in any scenario where motors interfere with other motors binding (i.e., motors already bound decrease the on-rate of other free motors; this is not considered explicitly below), the presence of the second MT will be even more beneficial, because for the case where some motors are bound to one MT, but none to the second, all of the "free" motors will have higher on-rates for the second MT.

Theoretical modeling confirms that multiple close microtubules likely improve transport

To test this hypothesis that the clustering of parallel MTs might improve transport in the multiple motor case, we investigated the motility of a cargo driven by kinesin molecules clustered at a single attachment point on the cargo surface. We decided to cluster the kinesin motors on the cargo surface for two reasons. First, there is weak experimental evidence for kinesin clustering (32). Second, previous simulations (16) find that if motors are randomly placed on large cargos, achieving a reasonable number of engaged motors (i.e., three to six) would require a large number of motors (50 to 100) to be present on the cargo, which appears inconsistent with biochemical characterizations of cargo-bound MT motors (33). Note that recent studies show that in vivo cargos are frequently moved by more than one MT-based motor (10,29,33,34). Our simulated 3D model (16) took into account the Brownian motion of the cargo as well as the positions of the motors and MTs. We considered transport when the cargo was close to either one or two MTs, and incorporated the wall effect by renormalizing the effective viscosity of the medium. A diagram of the simulated geometry for multiple MT transport in an axon is depicted in Fig. S1. We fixed the position of the MTs symmetrically about the center of the axon, parallel to the axis of the axon, and let one of the motors bind to either of the two MTs randomly. The binding process, the position of the cargo and the diameter of the axon all satisfied the boundary conditions that were described above for a

single MT. Initially, one motor was allowed to bind the MT and the rest were free. The algorithmic details of the motor processivity and switching between the MTs are described in the Supporting Material.

In Fig. 3, we show the run lengths, i.e., travel distances, of a cargo with $N = 2$ to 5 kinesin motors, moving along two parallel MTs, separated by MT center-to-center distances of $d = 50$, 75, and 275 nm as a function of viscosity. For simplicity, as discussed above, we assumed that the effect of axonal wall and/or the cargo-protein interactions was to modify the effective viscosity of the axoplasm. The MT separation of $d = 275$ nm approximately corresponded to the case of single MT transport since two kinesin motors, each 110 nm long and attached at a single point on the cargo, cannot reach two MTs simultaneously. In contrast, the motors could easily reach both MTs for the case of $d = 75$ nm. As we show in the next section, finding two MTs within 75 nm of each other is highly likely in small-caliber axons where the MT density is 150 MTs/μm^2 (3–6). It is evident that the second MT significantly enhanced the mean travel distance of the cargo, and the larger the number of motors, the stronger the enhancement.

The extreme values of the viscosity considered in some parts of the curves in Fig. 3 (>1000 × that of water), in general likely do not reflect what occurs in typical axoplasm. However, we demonstrated in an earlier section that under certain conditions (e.g., for the special class of cargo-axon geometry, $h/a \leq 1$), the resistance to motion could be tremendously large. In such cases, clustering the MTs within a high load region of the axon might be a potential mechanism to overcome resistance to transport.

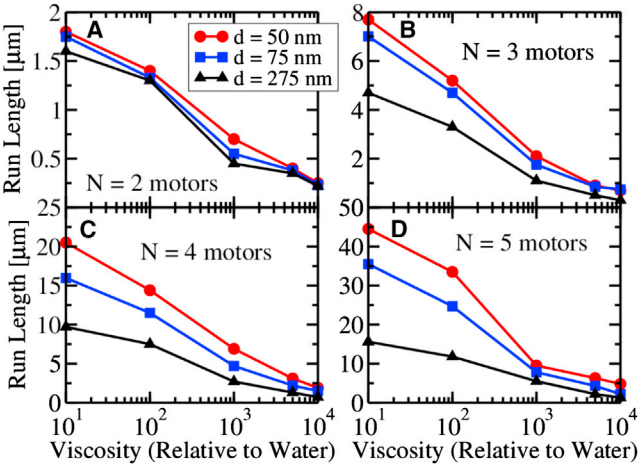

FIGURE 3 Cargo run length (i.e., cargo travel distance) along two parallel microtubules as a function of viscosity for a cargo (radius $a = 100$ nm) driven by a maximum of (*A*) $N = 2$ motors, (*B*) $N = 3$ motors, (*C*) $N = 4$ motors, and (*D*) $N = 5$ motors. For each number of (maximally engaged) motors, we investigated different microtubule-microtubule spacings d. The two microtubules were separated by center-to-center distances of $d = 50$ nm (*upper curve*); $d = 75$ nm (*middle curve*); and $d = 275$ nm (*lower curve*). To see this figure in color, go online.

How close do the parallel MTs need to be to each other to effectively contribute to transport? Since a factor of 10 enhancement (because of wall effects and large molecules) over the base axonal viscosity (10 times that of water (9)) seemed reasonable from our above studies, we used this, and compared the run lengths, i.e., travel distances, of a cargo hauled by different numbers of motors, as a function of spacing between the MTs. As Fig. 4 shows, the enhancement of run length by decreasing MT separation for a small number of motors ($N = 2$) was not dramatic, even when the spacing between the MTs was very small. However, for a larger number of motors, the second MT had a considerable impact. For example, when five motors were present, there was almost a threefold enhancement of the run length as compared with the single MT value if the MT separation was ~ 50 nm. The enhancement of the run length was significantly higher when the separation between the MTs was ~ 100 nm or less.

High microtubule density in small-caliber axons ensures closely spaced MTs that can be used in cargo transport to overcome the wall effect

To overcome the enhanced viscosity because of the wall effect in small-caliber axons, our simulation results suggested that nearest-neighbor MTs should be spaced within ~ 100 nm of each other so that both can effectively contribute to transport of a given cargo. (In large-caliber axons, the cargos are not subjected to the wall effect because they are sufficiently far away from the axonal wall.) If an axon has MTs randomly placed according to a Poisson distribution, how high does the MT density need to be to have a high probability of finding a pair of MTs within a certain distance? The answer is shown in Fig. 5 where we see that

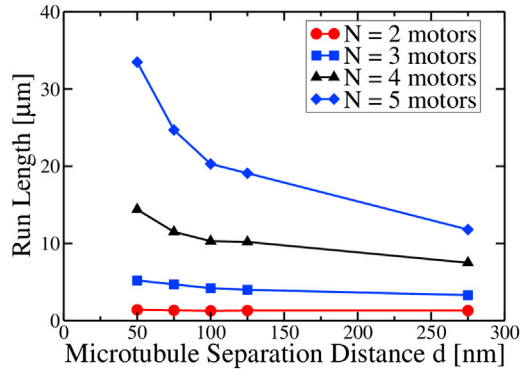

FIGURE 4 Cargo run length (i.e., cargo travel distance) as a function of the microtubule center-to-center separation for different numbers of motors. There are two microtubules. N is the number of motors on the cargo. Here the cargo radius is $a = 100$ nm, and the viscosity is 100 times that of water. In the simulations, a single motor binds to one of the microtubules and the system then evolves. The additional (free) motors can bind to either microtubule, governed by the prescribed binding rules implemented in the simulation (see the Supporting Material). To see this figure in color, go online.

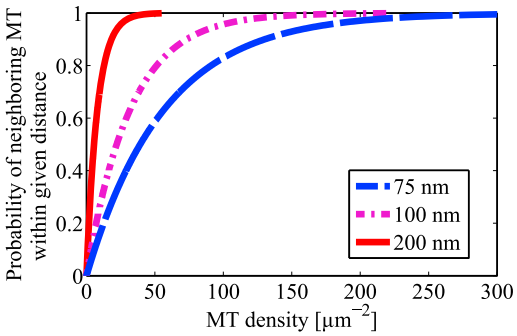

FIGURE 5 Probability of an MT having a neighbor within a given distance d versus MT density, where $d = 75$, 100, and 200 nm. Note that to have at least an 80% chance of having a pair of MTs with a separation of 75 nm (*blue dashed line*), the axon needs to have an MT density of ~ 100 MTs/μm^2. To see this figure in color, go online.

to have at least an 80% chance of having a pair of MTs with a separation of 75 nm, the axon needs to have an MT density of ~ 100 MTs/μm^2. Thus the observation of 150 MTs/μm^2 of cross-sectional area of axoplasm for small unmyelinated axons (3–6) means that small-caliber axons will have a high chance of having MTs with a spacing of less than 100 μm. Note that in axoplasm of large unmyelinated axons of ~ 10 μm in diameter, the MT density is less than 15 MTs/μm^2 (6), which implies that large-caliber axons with randomly placed MTs will have a rather low change of having MTs within 100 nm of each other and thus, cargo transport will tend to occur along single MTs. This is fine since the cargos in such large-caliber axons will not encounter the wall effect.

DISCUSSION

Axonal transport and its failure are of substantial interest with regard to neurodegeneration and neuropathy. In this study, we suggest that in small-caliber axons, the effect of the wall can be significant. Importantly, the effect is highly nonlinear, depending on the distance between the cargo to the wall, as well as on the size of the cargo; when $h/a \sim 1$, the wall effect can dramatically increase opposition to motion.

We modeled the axonal membrane as a rigid wall even though one might expect it to be somewhat flexible and elastic, especially in unmyelinated axons. (Myelinated axonal membranes are more rigid because they are reinforced by the myelin sheath.) However, we believe that our approximation is reasonable for two reasons. First, Shlomovitz et al. have done microrheological measurements of the viscosity of in vitro phospholipid monolayers in which micron sized beads submerged a fixed distance beneath the monolayer are shaken parallel to the monolayer in an optical trap (35). The viscous drag experienced by the beads can be used to infer the viscosity or rigidity of the monolayer membrane. For membrane viscosities less than 10^{-9} N·s/m with the bead at a depth corresponding to barely touching the monolayer, the hydrodynamic forces on the bead produced by the monolayer are like that of a free fluid. For membrane viscosities greater than ~ 4×10^{-7} N·s/m at a depth corresponding to barely touching the membrane, they find that the hydrodynamic forces produced by the membrane on the bead are like that of a rigid wall and show no evidence of membrane deformation. The rigid-wall membrane viscosity of 4×10^{-7} N·s/m is comparable with that of cellular membranes. For example, for erythrocytes the measured values of the membrane viscosity vary; it has been measured to be 3.4×10^{-7} N·s/m when high frequency electric fields induced transient deformation (36), and to be 3×10^{-6} N·s/m when a membrane tether was extruded (37). In another example, the membrane viscosity of a neuronal growth cone has been measured to be 2×10^{-7} N·s/m from studies where membrane tethers that were sliding over the cortical cytoskeleton were extruded (38). Even though 2×10^{-7} N·s/m is less than 4×10^{-7} N·s/m, Shlomovitz et al. still found significantly enhanced hydrodynamic drag at this value because of the presence of the membrane and no evidence of membrane deformation.

Second, cortical cytoskeletal filaments underlie the axonal membrane, increasing its effective stiffness. Importantly, very recent work by Xu et al. (39) found that actin forms ringlike structures that wrap around the circumference of axons and are evenly spaced along axonal shafts with a periodicity of ~ 180 to 190 nm. The cytoskeletal protein spectrin also exhibited periodic structures alternating with those of the actin rings, and the distance between adjacent actin rings was comparable with the length of a spectrin tetramer (39). Thus, for a cargo to deform the membrane, it must also deform the underlying actin-spectrin-based cytoskeleton. Thus we believe that our approximation of the axonal membrane as a rigid wall is reasonable. Such a wall would provide opposition to cargos moving in close proximity to the wall. The point of this paper is to point this out, and to encourage experiments to test this hypothesis.

One would expect viscous drag to slow intracellular transport velocity with increasing vesicle size. This has been seen in axonal transport in the giant squid axon (0.5 mm diameter) where small vesicles, that typically had apparent diameters of 0.1 to 0.2 μm, had faster mean velocities (2.5 μm/s) than medium-sized (0.2 to 0.6 μm) and large (greater than 0.6 μm) vesicles (40). Another published example of size-dependent opposition to motion involves LIS1, which is a protein that enables dynein to produce sustained force generation (41). Inhibition of LIS1 arrested the motion of large lysosomes/late endosomes in axonal transport but had little effect on the transport of small vesicles (19). Importantly, these effects were not observed in nonneuronal cells (19), which is consistent with LIS1 playing a role in transport under high resistance conditions.

However, viscous drag is not the only factor that can affect axonal transport, as implied by the broad distribution of velocities of similar-sized cargos, as well as the observation that anterograde motion tended to be more rapid than retrograde motion (40).

We suggested above that closely spaced pairs of MTs that result from high densities of randomly placed MTs in small-caliber axons can allow cargos to engage simultaneously motors on more than one MT. In an axon either the MTs are clustered or they are not. It may be that they are clustered in some axons as has been reported (23,42,43), and are not clustered in others as in the examples shown in the Supporting Material. If they are clustered, then there will be MTs within 100 nm of other MTs, by the definition of clustering. If they are not clustered but the MT density is high enough, then there is a very high probability that there will be at least two MTs within 100 nm of each other. Either way, clustered or not, there will be closely spaced MTs if the MT density is high enough in an axon. As we point out above, the MT density (3–6) is indeed high enough in small-caliber axons but not in large-caliber axons where our theory suggests that the wall effect does not hinder transport because the transported vesicles tend to be far from the axonal wall.

With regard to the mechanism that leads to a high density of MTs in small-diameter axons and a low MT density in large-caliber axons, we can say the following. Both neurofilaments (NFs) and MTs are found oriented along the length of axons, and the total number of neurofilaments and MTs together seems to be proportional to the diameter of the axon (43). Large-caliber axons are dominated by neurofilaments with roughly 5 to 10 times more NFs than MTs (44). As axons become smaller in diameter, this ratio decreases as the neurofilaments become fewer and less prominent, until in thin unmyelinated axons, neurofilaments are rare, leaving only a high density of MTs (6,43). Axon diameter decreases as axons branch. One can also follow the radial growth of axons after birth. After birth, peripheral nerves are small and unmyelinated (45). In mice, myelination is completed around postnatal day 21 (46). An axon that is fated to be 12 μm in diameter is ~ 1 μm at birth (47). Radial growth will begin once myelination is complete (48). During this time of growth from 1 μm to 12 μm, neurofilaments will become the predominant cytoskeletal proteins, leading to a dilution of the MT density and the observed low density of MTs in large-caliber axons (43,44).

MTs that are close together can be used to improve motor function, by increasing each motor's "on" rate, and thus, on average, increasing the average number of engaged motors at any instant. Several groups have suggested that the velocity of a cargo is determined by the number of motors hauling it for a given viscous drag (49–52). For a single motor, force-velocity curves show that the velocity decreases with increasing load on the motor (53–55), though in vitro measurements (55) indicate that the load on the motor needs to exceed ~ 2 pN before there is a noticeable reduction of the velocity. Klump and Lipowsky (49) have suggested that the load resulting from high cytoplasmic viscosity could decrease the travel distance and velocity of cargos, and that the velocity of such cargos depends on the number of motors and the external load on the cargo. The observation that a given cargo can change its velocity during the course of its travel and that intracellular cargos of a given type have a distribution of velocities has led to the suggestion that velocity increases with the number of motors on a cargo to overcome the cytoplasmic viscous drag (50–52). However, Shubeita et al. (10) showed that reducing the number of engaged motors on lipid droplets in a *Drosophila* embryo changes neither the run lengths nor the velocities, implying that cytosolic drag in nonneuronal cells does not significantly limit transport. They found average plus-end transport velocities for lipid droplets were ~ 550 nm/s, and average minus end velocities were ~ 730 nm/s. This is comparable with average velocities in Chinese hamster ovary (CHO) cells of ~ 1 μm/s in both plus and minus end directions for vesicles ranging in diameter from 30 to 300 nm (56). Average fast axonal transport speeds of mitochondria range from 1.4 μm/s (retrograde) and 1 μm/s (anterograde) in mice (57) to 0.4 μm/s in both directions in dorsal root ganglion cells (58). Thus a variety of cargo types and sizes are transported at roughly the same average speed, implying that cytosolic drag is not a limiting factor in intracellular transport.

However, in small-caliber axons, we hypothesize that the viscosity near the membrane is significantly increased, to the extent that it can hinder transport. We hypothesize that fast axonal transport rates are not lower in axons with small calibers because these axons have a higher density of MTs. Experimental studies involving radioactively labeled proteins have found that the rate of fast axonal transport in motor and sensory sciatic mammalian nerves of the cat, monkey, dog, rabbit, goat, and rat is ~ 400 mm/day (59). These nerves consist of bundles of myelinated axons. Cross-sections of sciatic nerves from cats taken at the wave front, or forward part of the crest of the wave, show radioactively labeled proteins in axons ranging in diameter from 3 to 23 μm (59). This suggests that the rate of fast axoplasmic transport is independent of the axon caliber over this range of diameters. Furthermore, it has been observed that the average number of mitochondria moving within mouse axons is independent of the axonal cross-sectional area for areas ranging from ~ 5 to 70 μm^2 (57), implying that on average, medium-caliber axons had many more mitochondria passing through a given volume of axoplasm than large-caliber axons. To test our assertion that fast axonal transport rates in small-caliber axons are comparable with those in large-caliber axons, there is a need for measurements of the speed of fast axonal transport in small axons with diameters of 1 μm or less. A further experimental test would be to knockdown the density of

MTs in small-caliber axons to see if the cargo velocities decrease because of the enhanced viscous drag of the membrane.

With these effects in mind, our study then suggests a number of related routes to the impairment of transport. First, impairing motor function, e.g., mutating the kinesin heavy chain (*Khc*) (60) or LIS1 inhibition (19) as we mentioned earlier, can obviously affect transport. Second, any perturbation that alters the paired MT structure would be expected to have significant consequences, because of decreased per-cargo motor utilization. Such a perturbation could arise from a decrease in overall MT density (e.g., because of tau impairment) or directly because of a change in the pair-spacing distance (likely controlled by MT-associated proteins). Third, a number of different classes of perturbations could contribute to alteration of the *h/a* ratio. Changes in the effective size of individual cargos (swollen lysosomes, various cargos that aberrantly stick together and form "clumps," etc.) could all increase the cargo radius *a*.

Similarly, any local constriction of the axon could result in decreasing the effective *h*. The diameter of myelinated feline axons decreases by 50% to 70% for a segment length of ~ 10 μm at the nodes of Ranvier (61,62). Berthold et al. observed that axoplasmic organelles accumulate in the paranode-node-paranode regions in large-caliber (diameter ~ 10 μm) myelinated axons of adult cats (63). At nodes of Ranvier in mouse axons, transported mitochondria often slow down and sometimes stall, especially those moving in the retrograde direction (57). When a mitochondrion is crossing a node, the average anterograde velocity is 0.7 μm/s compared with 1 μm/s without the node, and the average retrograde velocity is 0.6 μm/s compared with 1.4 μm/s in the absence of the node (57). Similar slowing of fast axonal transport in the vicinity of the node was observed for mitochondria being transported in small myelinated rat central nervous system axons where the average velocity in the internodal region was 0.47 μm/s in the anterograde direction compared with 0.27 μm/s in the nodal region, and 0.52 μm/s in the retrograde direction in the internodal region compared with 0.29 μm/s in the nodal region (64). Interestingly, in myelinated cat ventral root axons ranging in diameter from ~ 1 to 12 μm, the MT density is ~ 4 times higher in the nodal regions than in the intermodal regions, whereas the neurofilament density is essentially the same in these regions (65). This is consistent with our assertion that a higher density of MTs is needed for axonal transport, to allow the engagement of additional motors to overcome the increased viscosity near the axonal membrane.

Further, any stalled cargos also result in other (passing) cargos being "pushed" into the wall, again decreasing *h*. The result is organelle traffic jams. Mutations in the *Drosophila* kinesin heavy chain (*Khc*) disrupt anterograde fast axonal transport and leads to the stalling of organelles that depend on kinesin. This in turn probably disrupts retrograde transport, resulting in organelle traffic jams consisting of vesicles, synaptic membrane proteins, mitochondria and prelysosomal organelles that cause a dramatic swelling of axons (60). Similar traffic jams in axons have resulted from mutations of the *Drosophila* kinesin light chain (*Klc*) (66).

This leads us to ask whether there is evidence of such transport impairment in neuropathy and neurodegeneration found in disease processes (67–69). Our work implies that the increased viscous drag produced by the wall effect could be a factor in neurodegenerative diseases afflicting small fibers such as diabetes mellitus, Fabry's disease, and chemotherapy-induced peripheral neuropathy (70). For example, it is known that the amount of material conveyed via fast axonal transport is reduced by ~ 20% in the peripheral nerves of diabetic rats (71–73). In addition there is a 20% reduction in the cross-sectional area of axons in the peripheral nerves of diabetic rats (74,75), though the MT density of 25 to 28 MTs/μm^2 did not change in 3 μm diameter axons from sural nerves when compared with wild type rats (75). It is possible that the reduction in axonal caliber increased the influence of the wall effect and contributed to the reduction in fast axonal transport. It is also possible that the impairment of transport contributed to the decrease in axonal caliber.

The purpose of this paper has been to point out that there can be significant viscous drag on cargos moving close to the axonal wall, which effectively acts as a rigid wall. We have used a simple model of axonal transport to illustrate this, and some ways in which the model of axonal transport could be enhanced are described in the Supporting Material. This work thus provides a useful conceptual framework for viscous boundary effects but the extent to which such scenarios contribute to disease progression in the animal remains to be explored experimentally.

SUPPORTING MATERIAL

Seven figures, three tables, and References (76–81) are available at http://www.biophysj.org/biophysj/supplemental/S0006-3495(14)00075-7.

We thank Nigel Calcutt for helpful discussions and for critically reading our manuscripts, and Charles Stevens for helpful discussions. CCY thanks the hospitality of the Aspen Center for Physics which is supported by the National Science Foundation under Grant No. PHYS-1066293.

This work was supported by NIH/NIGMS grant number 5R01GM079156 to C. C. Yu and S. P. Gross.

REFERENCES

1. De Vos, K. J., A. J. Grierson, …, C. C. Miller. 2008. Role of axonal transport in neurodegenerative diseases. *Annu. Rev. Neurosci.* 31:151–173.

2. Morfini, G. A., M. Burns, …, S. T. Brady. 2009. Axonal transport defects in neurodegenerative diseases. *J. Neurosci.* 29:12776–12786.

3. Fadić, R., J. Vergara, and J. Alvarez. 1985. Microtubules and caliber of central and peripheral processes of sensory axons. *J. Comp. Neurol.* 236:258–264.
4. Pannese, E., M. Ledda, …, P. Procacci. 1984. A comparison of the density of microtubules in the central and peripheral axonal branches of the pseudounipolar neurons of lizard spinal ganglia. *Anat. Rec.* 208:595–605.
5. Malbouisson, A. M., M. N. Ghabriel, and G. Allt. 1985. Axonal microtubules: a computer-linked quantitative analysis. *Anat. Embryol. (Berl.).* 171:339–344.
6. Peters, A., S. L. Palay, and H. D. Webster. 1991. The Fine Structure of the Nervous System: Neurons and Their Supporting Cells. Oxford University Press, New York.
7. Biondi, R. J., M. J. Levy, and P. A. Weiss. 1972. An engineering study of the peristaltic drive of axonal flow. *Proc. Natl. Acad. Sci. USA.* 69:1732–1736.
8. Gilbert, D. L., W. J. Adelman, and J. M. Arnold. 1990. Squid as Experimental Animals. Plenum Press, New York.
9. Haak, R. A., F. W. Kleinhans, and S. Ochs. 1976. The viscosity of mammalian nerve axoplasm measured by electron spin resonance. *J. Physiol.* 263:115–137.
10. Shubeita, G. T., S. L. Tran, …, S. P. Gross. 2008. Consequences of motor copy number on the intracellular transport of kinesin-1-driven lipid droplets. *Cell.* 135:1098–1107.
11. Happel, J., and H. Brenner. 1965. Low Reynolds Number Hydrodynamics, with Special Applications to Particulate Media. Prentice-Hall, Englewood Cliffs, NJ.
12. Haberman, W. L., and R. M. Sayre. 1958. Motion of Rigid and Fluid Spheres in Stationary and Moving Liquids Inside Cylindrical Tubes. David Taylor Model Basin. Report No. 1143. Department of the U.S. Navy, Washington, DC.
13. Tozeren, H. 1983. Drag on eccentrically positioned spheres translating and rotating in tubes. *J. Fluid Mech.* 129:77–90.
14. Brenner, H., and J. Happel. 1958. Slow viscous flow past a sphere in a cylindrical tube. *J. Fluid Mech.* 4:195–213.
15. Greenstein, T., and J. Happel. 1968. Theoretical study of the slow motion of a sphere and a fluid in a cylindrical tube. *J. Fluid Mech.* 34:705–710.
16. Erickson, R. P., Z. Jia, …, C. C. Yu. 2011. How molecular motors are arranged on a cargo is important for vesicular transport. *PLOS Comput. Biol.* 7:e1002032.
17. Tang-Schomer, M. D., A. R. Patel, …, D. H. Smith. 2010. Mechanical breaking of microtubules in axons during dynamic stretch injury underlies delayed elasticity, microtubule disassembly, and axon degeneration. *FASEB J.* 24:1401–1410.
18. Kunwar, A., M. Vershinin, …, S. P. Gross. 2008. Stepping, strain gating, and an unexpected force-velocity curve for multiple-motor-based transport. *Curr. Biol.* 18:1173–1183.
19. Yi, J. Y., K. M. Ori-McKenney, …, R. B. Vallee. 2011. High-resolution imaging reveals indirect coordination of opposite motors and a role for LIS1 in high-load axonal transport. *J. Cell Biol.* 195:193–201.
20. Kaasik, A., D. Safiulina, …, V. Veksler. 2007. Regulation of mitochondrial matrix volume. *Am. J. Physiol. Cell Physiol.* 292:C157–C163.
21. Voter, W. A., and H. P. Erickson. 1982. Electron microscopy of MAP 2 (microtubule-associated protein 2). *J. Ultrastruct. Res.* 80:374–382.
22. Mukhopadhyay, R., S. Kumar, and J. H. Hoh. 2004. Molecular mechanisms for organizing the neuronal cytoskeleton. *BioEssays.* 26:1017–1025.
23. Hirokawa, N. 1982. Cross-linker system between neurofilaments, microtubules, and membranous organelles in frog axons revealed by the quick-freeze, deep-etching method. *J. Cell Biol.* 94:129–142.
24. Hirokawa, N., S. Hisanaga, and Y. Shiomura. 1988. MAP2 is a component of crossbridges between microtubules and neurofilaments in the neuronal cytoskeleton: quick-freeze, deep-etch immunoelectron microscopy and reconstitution studies. *J. Neurosci.* 8:2769–2779.
25. Wiche, G., and L. Winter. 2011. Plectin isoforms as organizers of intermediate filament cytoarchitecture. *BioArchitecture.* 1:14–20.
26. Fuchs, P., M. Zörer, …, G. Wiche. 2009. Targeted inactivation of a developmentally regulated neural plectin isoform (plectin 1c) in mice leads to reduced motor nerve conduction velocity. *J. Biol. Chem.* 284:26502–26509.
27. Mallik, R., D. Petrov, …, S. P. Gross. 2005. Building complexity: an in vitro study of cytoplasmic dynein with in vivo implications. *Curr. Biol.* 15:2075–2085.
28. Driver, J. W., D. K. Jamison, …, M. R. Diehl. 2011. Productive cooperation among processive motors depends inversely on their mechanochemical efficiency. *Biophys. J.* 101:386–395.
29. Mallik, R., and S. P. Gross. 2009. Intracellular transport: how do motors work together? *Curr. Biol.* 19:R416–R418.
30. Gross, S. P., M. A. Welte, …, E. F. Wieschaus. 2002. Coordination of opposite-polarity microtubule motors. *J. Cell Biol.* 156:715–724.
31. Müller, M. J., S. Klumpp, and R. Lipowsky. 2008. Tug-of-war as a cooperative mechanism for bidirectional cargo transport by molecular motors. *Proc. Natl. Acad. Sci. USA.* 105:4609–4614.
32. Gross, S. P., M. Vershinin, and G. T. Shubeita. 2007. Cargo transport: two motors are sometimes better than one. *Curr. Biol.* 17:R478–R486.
33. Hendricks, A. G., E. Perlson, …, E. L. Holzbaur. 2010. Motor coordination via a tug-of-war mechanism drives bidirectional vesicle transport. *Curr. Biol.* 20:697–702.
34. Soppina, V., A. K. Rai, …, R. Mallik. 2009. Tug-of-war between dissimilar teams of microtubule motors regulates transport and fission of endosomes. *Proc. Natl. Acad. Sci. USA.* 106:19381–19386.
35. Shlomovitz, R., A. A. Evans, …, A. J. Levine. 2013. Measurement of monolayer viscosity using noncontact microrheology. *Phys. Rev. Lett.* 110:137802.
36. Engelhardt, H., and E. Sackmann. 1988. On the measurement of shear elastic moduli and viscosities of erythrocyte plasma membranes by transient deformation in high frequency electric fields. *Biophys. J.* 54:495–508.
37. Hochmuth, R. M., H. C. Wiles, …, J. T. McCown. 1982. Extensional flow of erythrocyte membrane from cell body to elastic tether. II. Experiment. *Biophys. J.* 39:83–89.
38. Dai, J., and M. P. Sheetz. 1995. Mechanical properties of neuronal growth cone membranes studied by tether formation with laser optical tweezers. *Biophys. J.* 68:988–996.
39. Xu, K., G. Zhong, and X. Zhuang. 2013. Actin, spectrin, and associated proteins form a periodic cytoskeletal structure in axons. *Science.* 339:452–456.
40. Allen, R. D., J. Metuzals, …, S. P. Gilbert. 1982. Fast axonal transport in squid giant axon. *Science.* 218:1127–1129.
41. McKenney, R. J., M. Vershinin, …, S. P. Gross. 2010. LIS1 and NudE induce a persistent dynein force-producing state. *Cell.* 141:304–314.
42. Yamada, K. M., B. S. Spooner, and N. K. Wessells. 1971. Ultrastructure and function of growth cones and axons of cultured nerve cells. *J. Cell Biol.* 49:614–635.
43. Friede, R. L., and T. Samorajski. 1970. Axon caliber related to neurofilaments and microtubules in sciatic nerve fibers of rats and mice. *Anat. Rec.* 167:379–387.
44. Lee, M. K., and D. W. Cleveland. 1996. Neuronal intermediate filaments. *Annu. Rev. Neurosci.* 19:187–217.
45. Jessen, K. R., and R. Mirsky. 1999. Schwann cells and their precursors emerge as major regulators of nerve development. *Trends Neurosci.* 22:402–410.
46. Agrawal, D., R. Hawk, …, D. A. Kirschner. 2009. Internodal myelination during development quantitated using x-ray diffraction. *J. Struct. Biol.* 168:521–526.
47. Nilsson, I., and C. H. Berthold. 1988. Axon classes and internodal growth in the ventral spinal root L7 of adult and developing cats. *J. Anat.* 156:71–96.

48. de Waegh, S. M., V. M. Lee, and S. T. Brady. 1992. Local modulation of neurofilament phosphorylation, axonal caliber, and slow axonal transport by myelinating Schwann cells. *Cell.* 68:451–463.

49. Klumpp, S., and R. Lipowsky. 2005. Cooperative cargo transport by several molecular motors. *Proc. Natl. Acad. Sci. USA.* 102:17284–17289.

50. Hill, D. B., M. J. Plaza, …, G. Holzwarth. 2004. Fast vesicle transport in PC12 neurites: velocities and forces. *Eur. Biophys. J.* 33:623–632.

51. Kural, C., H. Kim, …, P. R. Selvin. 2005. Kinesin and dynein move a peroxisome in vivo: a tug-of-war or coordinated movement? *Science.* 308:1469–1472.

52. Levi, V., A. S. Serpinskaya, …, V. Gelfand. 2006. Organelle transport along microtubules in *Xenopus melanophores*: evidence for cooperation between multiple motors. *Biophys. J.* 90:318–327.

53. Visscher, K., M. J. Schnitzer, and S. M. Block. 1999. Single kinesin molecules studied with a molecular force clamp. *Nature.* 400:184–189.

54. Singh, M. P., R. Mallik, …, C. C. Yu. 2005. Monte Carlo modeling of single-molecule cytoplasmic dynein. *Proc. Natl. Acad. Sci. USA.* 102:12059–12064.

55. Schnitzer, M. J., K. Visscher, and S. M. Block. 2000. Force production by single kinesin motors. *Nat. Cell Biol.* 2:718–723.

56. Trinczek, B., A. Ebneth, …, E. Mandelkow. 1999. Tau regulates the attachment/detachment but not the speed of motors in microtubule-dependent transport of single vesicles and organelles. *J. Cell Sci.* 112:2355–2367.

57. Misgeld, T., M. Kerschensteiner, …, J. W. Lichtman. 2007. Imaging axonal transport of mitochondria in vivo. *Nat. Methods.* 4:559–561.

58. Perrot, R., and J. P. Julien. 2009. Real-time imaging reveals defects of fast axonal transport induced by disorganization of intermediate filaments. *FASEB J.* 23:3213–3225.

59. Ochs, S. 1972. Rate of fast axoplasmic transport in mammalian nerve fibres. *J. Physiol.* 227:627–645.

60. Hurd, D. D., and W. M. Saxton. 1996. Kinesin mutations cause motor neuron disease phenotypes by disrupting fast axonal transport in *Drosophila*. *Genetics.* 144:1075–1085.

61. Rydmark, M. 1981. Nodal axon diameter correlates linearly with internodal axon diameter in spinal roots of the cat. *Neurosci. Lett.* 24:247–250.

62. Okamura, Y., and S. Tsukita. 1986. Morphology of freeze-substituted myelinated axon in mouse peripheral nerves. *Brain Res.* 383:146–158.

63. Berthold, C. H., C. Fabricius, …, B. Andersén. 1993. Axoplasmic organelles at nodes of Ranvier. I. Occurrence and distribution in large myelinated spinal root axons of the adult cat. *J. Neurocytol.* 22:925–940.

64. Ohno, N., G. J. Kidd, …, B. D. Trapp. 2011. Myelination and axonal electrical activity modulate the distribution and motility of mitochondria at CNS nodes of Ranvier. *J. Neurosci.* 31:7249–7258.

65. Berthold, C. H., and M. Rydmark. 1995. Morphology of normal peripheral axons. *In* The Axon: Structure, Function and Pathophysiology. S. G. Waxman, J. D. Kocsis, and P. K. Stys, editors. Oxford University Press, New York, pp. 13–48.

66. Gindhart, Jr., J. G., C. J. Desai, …, L. S. Goldstein. 1998. Kinesin light chains are essential for axonal transport in *Drosophila*. *J. Cell Biol.* 141:443–454.

67. Falnikar, A., and P. W. Baas. 2009. Critical roles for microtubules in axonal development and disease. *Results Probl. Cell Differ.* 48:47–64.

68. Bilsland, L. G., E. Sahai, …, G. Schiavo. 2010. Deficits in axonal transport precede ALS symptoms in vivo. *Proc. Natl. Acad. Sci. USA.* 107:20523–20528.

69. Williamson, T. L., and D. W. Cleveland. 1999. Slowing of axonal transport is a very early event in the toxicity of ALS-linked SOD1 mutants to motor neurons. *Nat. Neurosci.* 2:50–56.

70. Hoitsma, E., J. P. Reulen, …, C. G. Faber. 2004. Small fiber neuropathy: a common and important clinical disorder. *J. Neurol. Sci.* 227:119–130.

71. Meiri, K. F., and W. G. McLean. 1982. Axonal transport of protein in motor fibres of experimentally diabetic rats—fast anterograde transport. *Brain Res.* 238:77–88.

72. Mayer, J. H., and D. R. Tomlinson. 1983. Axonal transport of cholinergic transmitter enzymes in vagus and sciatic nerves of rats with acute experimental diabetes mellitus; correlation with motor nerve conduction velocity and effects of insulin. *Neuroscience.* 9:951–957.

73. Schmidt, R. E., F. M. Matschinsky, …, D. B. McDougal, Jr. 1975. Fast and slow axoplasmic flow in sciatic nerve of diabetic rats. *Diabetes.* 24:1081–1085.

74. Jakobsen, J. 1976. Axonal dwindling in early experimental diabetes. I. A study of cross sectioned nerves. *Diabetologia.* 12:539–546.

75. Iturriaga, R. 1985. Microtubule density and size of axons in early diabetes: implications for nerve cell homeostasis. *Exp. Neurol.* 88: 165–175.

76. Bungay, P. M., and H. Brenner. 1973. The motion of a closely-fitting sphere in a fluid-filled tube. *Int. J. Multiphase Flow.* 1:25–56.

77. Tozeren, H. 1982. Torque on eccentric spheres flowing in tubes. *J. Appl. Mech.-Trans. ASME.* 49:279–283.

78. Block, S. M., L. S. Goldstein, and B. J. Schnapp. 1990. Bead movement by single kinesin molecules studied with optical tweezers. *Nature.* 348: 348–352.

79. Hansen, J.-P., and I. R. McDonald. 1990. Theory of Simple Liquids. Academic Press, London.

80. Zar, J. H. 1974. Biostatistical Analysis. Prentice-Hall, Englewood Cliffs, NJ.

81. Zwillinger, D. 2003. CRC Standard Mathematical Tables and Formulae. CRC Press, Boca Raton, FL.

82. Ambari, A., B. Gauthier-Manuel, and E. Guyon. 1984. Wall effects on a sphere translating at constant velocity. *J. Fluid Mech.* 149:235–253.

Supporting Material for

Axonal Transport: How High Microtubule Density Can Compensate for Boundary Effects in Small-Caliber Axons

Juliana C. Wortman,[†] Uttam M. Shrestha,[†] Devin M. Barry,[‡] Michael L. Garcia,[§] Steven P. Gross,[†¶] and Clare C. Yu[†]*

[†]Department of Physics and Astronomy, University of California, Irvine, Irvine, CA 92697; [‡]Center for the Study of Itch, Washington University School of Medicine, St. Louis, MO 63110; [§]Biological Sciences, University of Missouri, Columbia, MO 65211; [¶]Department of Developmental and Cell Biology, University of California, Irvine, Irvine, CA 92697.

In this supplement, we describe the basic algorithm that we have used to simulate the cargo dynamics in multiple microtubules as well as the implementation of cargo-protein interactions. We also describe how we analyzed electron micrographs to obtain the distribution of microtubules. In Section 1, we describe the formalism of the wall effect. In Section 2, we introduce the transport of a cargo in multiple microtubules. In Section 3, we show the detail calculations of cargo-protein interactions. In Section 4, we show our simulation results of (1) the wall effect on a cargo transported by a single motor, and (2) the effective viscosity on a sphere being pushed through a cylinder containing a fluid with macromolecules. In Section 5, we show that large loads on the motor (when it is greatly extended) occur when the cargo is near the microtubule and far from the axon wall. In Section 6, we show how we analyzed the electron micrographs of axon cross sections to determine whether the distribution of microtubules is given by the Poisson distribution. In Section 7, we describe some ways to make our simulation more realistic.

1. Wall correction: Heuristic Approach

1.1 Effect on Translational Motion

Generally, the axoplasm has a viscosity that can be an order of magnitude larger than the viscosity of the water. The dynamical viscosity may be enhanced further due to the relative motion between the cargo and the axonal wall. In order to incorporate the wall effect quantitatively, let us consider translation of a spherical cargo of radius a moving in a cylindrical axon of radius R (Fig. 1 in main paper). We assume the viscosity of the axoplasm in an unbounded medium is η_0. Due to the finite size effect, the Stokes force experienced by the cargo moving with velocity $\boldsymbol{v}$ in the laboratory frame of reference is modified and can be expressed as in Eq. 1 in the main paper (1):

$$\boldsymbol{F} = 6\pi\eta_\infty a\boldsymbol{v}\, K(\boldsymbol{x}),$$

where $K(\boldsymbol{x})(\geq 1)$ is the correction factor due to the boundary wall effect and $\boldsymbol{x}$ is the position of the cargo. Here we assume the velocity of the cargo in the direction parallel to the axis of the axon tube. $K(\boldsymbol{x})$, in principle, depends on the position $\boldsymbol{x}$, the radius a of the cargo, and the diameter D of the axon.

The exact solution for the correction factor, $K(\boldsymbol{x})$, for a sphere moving along the axis of a cylinder filled with viscous fluid has been obtained numerically by solving a set of linear equations (1, 2).

Brenner and Happel, by employing the method of images, have given an asymptotic solution for a sphere positioned arbitrarily and eccentrically about the axis of the cylinder (3). However, those solutions are valid in the limit when the radius of the sphere is much smaller than to the size of the cylinder, and the sphere is not far from the axis. When the size of the sphere is comparable to that of the cylinder, Bungay and Brenner (4), and Tozeren (5) have provided approximate off-axis solutions perturbatively in terms of the eccentricity parameter that can be treated as small expansion coefficient,

$$\varepsilon = \frac{b}{R}$$

where b is the distance of the center of the sphere from the axis of the cylinder and R is the radius of the cylinder (Fig. 1 in main paper). All of the findings indicate that the viscous drag does not increase monotonically as ε increases. Instead, it reaches its minimum value around ε = 0.4, and then increases sharply afterwards. In fact this theoretical prediction has been verified experimentally in the optical feedback system and in circular conduits (6).

To the best of our knowledge, there is no converging general solution for $K(\boldsymbol{x})$ that applies over the entire range of possible positions and sizes of the sphere. For a rigid wall, the no-slip boundary condition dictates that the velocity of the sphere should tend to vanish when it approaches to the wall. This implies an infinite viscous drag and the functional behavior of the correction factor can be approximated as $K \sim 1/h$ for $h \to 0$, where h is the surface-to-surface distance of the sphere from the wall. By exploiting the behavior of the solutions near the axis and near the wall, we can heuristically write an approximate solution as a superposition, which is presumably valid over the entire range for 0 < ε < 1. Noting the fact that the off-axis viscous drag also depends upon the ratio of the radius of the sphere to the radius of the cylinder

$$k = \frac{a}{R},$$

Ambari (6) presented the experimental data for the correction term as a function of ε for different values of k. In order to fit these experimental data, we write the correction term in the form shown below and in Eq. 2 in the main text.

$$K = \exp(-k\varepsilon)\, K_0 + k^2\varepsilon^2\ f(\varepsilon)\,(R/h)$$

Here, K_0 is the wall correction factor for rigid spheres moving in a still liquid along the axis of a cylindrical tube (b = 0), and $f(\varepsilon)$ is an eccentricity function (1, 3), and h is the sphere-cylinder surface to surface distance. For the correction factor K_0, we use

$$K_0 = \frac{1 - 0.75857k^5}{1 - 2.1050k + 2.0865k^5 + 0.72603k^6}$$

When ε is near zero (i.e., the sphere is near the cylinder's axis), we make the approximation

$$f(\varepsilon) = 2.10444 - 0.6977\varepsilon^2$$

For values of ε near 1 (corresponding to a sphere near the cylinder wall), we use

$$f(\varepsilon) = \frac{9}{16(1-\varepsilon)}$$

It is evident that the heuristic correction recovers the previous results for both the limiting cases $\varepsilon \to 0$ and $h \to 0$. We have verified that our heuristic calculations are in agreement with the experimental results given by Ambari (6) as shown in Figure 1*C*.

In Fig. 1 in the main text, we show the correction factor *K* as a function of sphere-cylinder surface to surface distance *h* for two values of *k*, namely $k = 0.1$ and $k = 0.5$, where the radius of the sphere was fixed at $a = 250$ nm, and *k* was altered by changing the radius of the axon. The Faxén correction (1) for the sphere of the same radius moving parallel to a planar surface is also shown. The heuristic calculation also agrees well with the Faxén correction for a large cylinder with the sphere far away from the wall. Two general features of our results are of interest. First, relatively close to the wall, the boundary effect is very large, and second, for cargos that are relatively large with respect to the caliber of the axon (i.e. roughly filling it by half), the "wall" effect is evident even quite far away from the wall. For example, if we think of $\eta_{eff} = K\eta_{\infty}$ as an effective viscosity, then η_{eff} can be 50 times that of water for $K = 5$ and $\eta_{\infty} = 10$ times that of water (7). Previous theoretical findings indicate that viscous drag does not increase monotonically as ε increases. Instead, the minimum value is about $\varepsilon \approx 0.4$ and then the drag increases sharply with increasing ε (1); this prediction has been verified experimentally in an optical feedback system and in cylindrical conduits (6). We tested our phenomenological calculations against the experimentally measured correction factor (6) and found good agreement as shown in Fig. 1*C*.

1.2 Effect on Rotational Motion

The moving sphere approaching near the wall may also rotate due to the velocity gradient in the flow, and the corresponding torque is given by (1)

$$\boldsymbol{\tau}_{wall} = -8\pi\eta a^3 \boldsymbol{\omega},$$

where **ω** is the angular velocity of the rotation due to presence of the wall. This torque should not be confused with the torque exerted by external forces such as the pull of the motor or thermal kicks. Due to axial symmetry there is no wall effect producing the rotational motion for a sphere moving along the axis of the cylinder. Following Greenstein and Happel (8) the frictional torque within the first order approximation can be written as,

$$\boldsymbol{\tau}_{wall} = -8\pi\eta a^2 g(\varepsilon) k^2 \boldsymbol{v} \times \boldsymbol{z},$$

where **z** is the unit vector along the axis of the cylinder, and $g(\varepsilon)$ is the rotational eccentricity function that satisfies

$$(1-\varepsilon^2)g(\varepsilon) \ll 1.$$

For a typical cargo size (a = 250 nm) and motor velocity (v = 800 nm/s) and in a medium with the viscosity of water, one can estimate that the magnitude of the rotational torque is of the order of $\tau_{wall} \sim 1$ pN·nm. However, the torque experienced by a similar cargo driven by a kinesin motor with a load of 1 pN force is about 250 pN·nm. So we henceforth neglect the wall effect on the rotational motion.

2. Modeling of Kinesin Motors

In this paper we use the three-dimensional Monte Carlo method, as outlined in the Ref. (9), to study the transport carried out by kinesin motors(s). In this model, we consider kinesin molecules bound to a spherical cargo (vesicle), and the heads of the motor(s) are free to search for a place to bind on the protofilaments of the microtubule (MT). All places on the MT are available for binding. Once the motor head can reach the MT, we use a motor binding rate of 2 s^{-1}. It should be pointed out that the diffusion of the head was not incorporated into our model. The rule for the binding of the head to the microtubule was dictated by where the tail of the motor was attached to the surface of the cargo - that is, if the tail-microtubule distance was less than the native (unstretched) motor length, the motor bound to the MT at a given rate of 2 s^{-1} in our simulation. Nonetheless, we expected thermal fluctuations of the cargo to play a significant role in the motor(s) abilities to reach (and bind to) the microtubules.

We ignored head-head dynamics of a motor, and as others have done, simply modeled kinesin as a single head that hopped from one binding site to the next with step size of d = 8 nm, moving toward the plus end of the MT. We model kinesin as a monomer with a single head that can hop from one binding site to the adjacent site with a step size of d = 8 nm towards the positive end of the MT. These motors exert an elastic force on an object only when they are stretched, not when they are compressed. In our model, the tails of the motors are always bound to the cargo. Motors can actively participate in the cargo hauling process only when they are engaged, i.e., bound to the MT. In the presence of ATP molecules, the stochastic stepping of the motors is governed by Michaelis-Menten kinetics (10). The stepping of the motors applies mechanical force to the cargo. In our model, the tails of the kinesins were always bound to the cargo while the head could bind the MT. The motors participated in the transport process only when they were engaged, i.e., bound to the MT. In addition to the forces acting on the cargo due to the molecular motors and viscous drag, it also underwent Brownian motion.

2.1 Kinesin Kinetic Cycle and Stepping

In order to introduce our notation and parameters, we briefly review in this subsection how the kinesin completes its kinetic cycle and exerts mechanical force on the cargo.

Kinesin moves processively towards the plus end of the MT by hydrolyzing ATP molecules. The velocity of the movement of the kinesin is determined by the rate of binding of ATP to the motor head and its subsequent hydrolysis,

$$K + ATP \rightleftharpoons (K \cdot ATP) \rightarrow K + ADP + P_i$$

We denote motor-ATP on (binding) and off (unbinding) rates by k_{on} and k_{off}, and the rate of the ATP hydrolysis by k_{cat}. After hydrolysis of ATP, ADP and the phosphate ion P_i are released. The motor stepping velocity is given by the Michaelis-Menten rate of the chemical reaction (11):

$$V = \frac{V_{max}[ATP]}{[ATP] + K_m}$$

where [*ATP*] is the ATP concentration and V_{max} is the maximum velocity at the saturated concentration of the ATP molecules which can be expressed in terms of the load dependent efficiency function, $\zeta(F)$, as

$$V_{max} = k_{cat} d \zeta(F),$$

where *F* is the external load on the motor. The efficiency function, $\zeta(F)$, is maximum at zero load and decays to zero at the motor stall force. We therefore write the approximation

$$\zeta(F) = \left(1 - \left(\frac{F}{F_0}\right)^2\right).$$

The Michaelis-Menten constant K_m is defined by

$$K_m = \frac{k_{cat} + k_{off}}{k_{on}}.$$

The off-rate of ATP from the motor head, in principle, also depends upon the applied load *F,* and can be scaled in terms of experimentally measurable parameters as

$$k_{off} = k_{off}^0 \exp\left(\frac{F\delta}{k_B T}\right),$$

where $k_B T$ is the thermal energy, δ is a characteristic length, and k_{off}^0 is the no load off-rate that can be fitted with the experimental results (12).

The finite value of the run length during the stochastic stepping of the kinesin implies a finite lifetime of the motor-MT bound state. We follow the detachment kinetics as discussed in (11) in order to quantify the rate of dissociation of kinesin molecules from the MT. The probability of the detaching from the MT per unit time before ($P_{detach1}$) and after ($P_{detach2}$) the ATP binds are defined as

$$P_{detach1} = \frac{BP_{step}}{[ATP]},$$

$$P_{detach2} = \frac{\exp(\mathrm{F}\frac{\delta_l}{k_B T})P_{step}}{A},$$

where

$$P_{step} = \frac{k_{cat}\zeta(F)[ATP]}{[ATP]+K_m}.$$

Here, δ_l, A and B are physical constants characteristic of the molecular motor, and can be fitted with the experimental data (12). Once the detachment rates are known, the probabilities that the motors dissociate from the MT in each Monte Carlo time step dt are $P_{detach1}dt$ and $P_{detach2}dt$ before and after the ATP binds. The motor detachment rate above stall is, however, constant.

The list of constant parameter values used in our simulations is given in Table S1.

Table S1: Parameters and Values for the Motor Simulation

Parameters	Values	Comments
δ	1.3 nm	Characteristic length
d	8 nm	Step
k_{on}	2 μM s^{-1}	ATP on-rate
k_{off}^0	55 s^{-1}	ATP off-rate
k_{cat}	105 s^{-1}	Rate of hydrolysis
$[ATP]$	2000 μM	ATP concentration
A	107	Constant
B	0.029 μM	Constant
l	110 nm	Motor length
k	0.32 pN/nm	Motor spring constant
T	300 K	Temperature
dt	$10^{-6}-10^{-5}$ s	Time step
r_{MT}	12.5 nm	Radius of MT
k_{off} (back-detach)	2 s^{-1}	Above stall-detachment rate

2.2 Cargo Dynamics

In a viscous medium, a cargo under the action of molecular motor(s) undergoes diffusive-directive motion. It is capable of translation as well as rotation due to the resultant Brownian kicks from the molecules in the medium.

For a given axonal cross section and MT position, we assume that the head of the kinesin molecule can bind to the MT at time $t = 0$. If the motor state is on, there is a certain waiting time between the motor binding and the ATP hydrolysis plus ADP release. Once the ATP is hydrolyzed, the motor head instantly takes a step forward of $d = 8$ nm towards the plus end of the MT. As the head steps forward, the motor gets stretched and exerts mechanical force on the cargo. Since the motion is highly overdamped, the time to reach the Stokes regime is much smaller than any relevant time scale in the system. The dynamics of the cargo is modeled by the Langevin equation,

$$m\frac{d}{dt}\boldsymbol{v}(t) = -\alpha_T \boldsymbol{v}(t) + \boldsymbol{f}^{ext}(t) + \boldsymbol{f}^{thermal}(t).$$

The first term on the right hand side is the drag force at the instant when the cargo is moving with velocity $\boldsymbol{v}(t)$, and the drag coefficient is given by

$$\alpha_T = 6\pi K(\boldsymbol{x})\eta_0 a,$$

where the correction factor $K(\boldsymbol{x})$ is given by Eq. (2) in the main paper, and $\boldsymbol{x}$ is the position of the cargo with respect to the wall. The second term is the sum of all external forces due to motor(s) and the confining potential (if any). The last term is the sum of the all forces due to the erratic kicks given by fluid molecules that give the cargo Brownian motion.

If we assume that the cargo to be in a state of mechanical equilibrium, the average velocity is a time independent quantity and we can integrate the above equation in the presence of thermal fluctuations to obtain the time evolution of the position of the center of mass of the cargo (9):

$$\boldsymbol{x}(t+\Delta t) = \boldsymbol{x}(t) + \frac{\Delta t}{\alpha_T}\boldsymbol{f}^{ext}(x,t) + \sigma_T \boldsymbol{\varepsilon}_T,$$

where we have defined

$$\sigma_T = \sqrt{\frac{2k_B T \Delta t}{\alpha_T}},$$

and $\boldsymbol{\varepsilon}_T$ is a three-dimensional random variate drawn from a normally distributed function of zero mean and unit standard deviation. An analogous equation can also be derived for the torque and the rotational motion of the cargo. The details of the calculation can be found in Ref. (9).

Throughout our simulation, the motor-cargo system satisfies the following boundary conditions: (i) the motor cannot enter into the cargo or the MT; (ii) the cargo cannot enter into the MT; and (iii) the cargo must lie inside the axon.

2.3 Implementation of Multiple Motors on Multiple Microtubules

It has been shown both in vitro and in vivo that the effective transport of a comparatively large cargo is, basically, carried out by several molecular motors (13). The multiple-motor transport is particularly important in a geometrically constrained cell such as a neuron since the undulations and constrictions of a long narrow axon could obstruct the motion significantly.

For a given cargo size, axon caliber, and MT position, multiple motor transport depends upon how the motors are distributed over the surface of the cargo. It also depends upon the state of the motors. For instance, if the motors are uniformly distributed over the surface of the cargo and if their density is low, the transport is basically associated with a single motor since only one motor at a time can access the MT. Multiple motor transport is also influenced by the initial binding state and the attachment rate of the motors to the MT. The higher the motor binding rate, the longer is the run length of the cargo.

In our two-MT-multiple-motor simulations, we fix the position of 2 MTs parallel to the axis of the axon and let one of the motors bind to either of the MTs randomly. The binding process, position of the cargo and the size of the axon all satisfy the boundary conditions mentioned before. It should be noted that the initial motor state, i.e., whether the motor is on (ATP-bound) or off (ATP-unbound) also affects the transport properties. In the simulations, we assume an ATP molecule is bound to the head of the motor at the time when the motor attaches to the MT. When transport starts, only one motor is allowed to bind to the MT and the rest of the motors are free. Multiple motor transport along a single MT is discussed in detail in Ref. (9). Here we describe briefly the scenario of multiple-motor transport along two MTs (see Fig. S1).

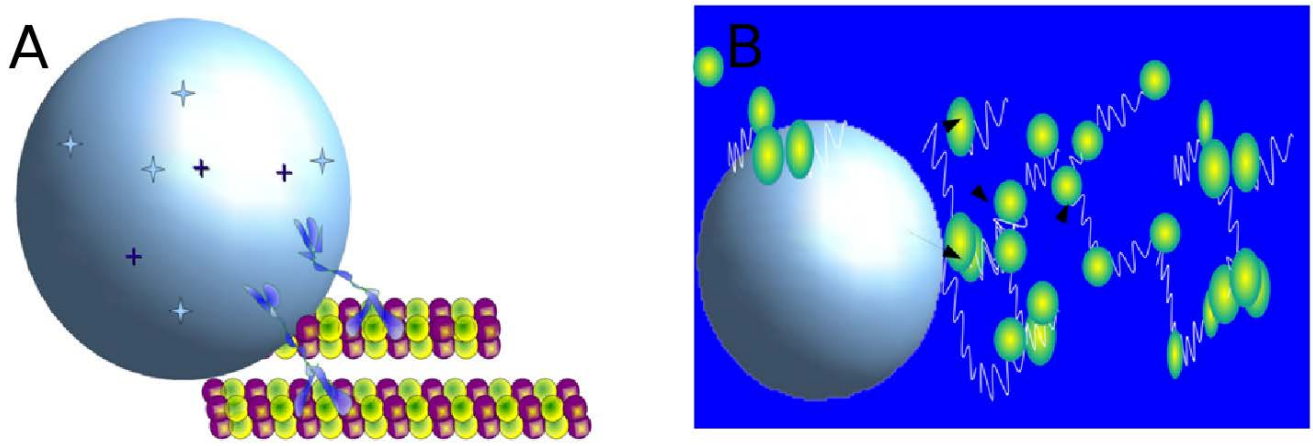

Figure S1: (*A*) A cartoon of a cargo being hauled by multiple motors along parallel microtubules. (*B*) Cargo interacting with polymers. A polymer is modeled by a chain of beads linked by tiny springs. Unlike the cargo, each bead of a polymer performs constrained diffusive motion.

Our simulation for the calculation of the run length goes as follows:

At $t = 0$, a given number of motors is specified.
A single motor is fixed at a point defined by spherical coordinate angles (θ, φ) on the surface of the cargo.
The tails of rest of the motors are distributed in a region from (θ, φ) to $(\theta + 0.01\pi, \varphi + 0.01\pi)$.
In other words, the tails of the motors are clustered together on the surface of the cargo.
At $t = 0$, a single motor is allowed to bind to one of the MTs to initiate the simulation.
At $t > 0$, the motors that can reach to the MT will be able to bind without bias at the binding rate of 2 per sec.

The binding of the motors to the second MT depends upon the MT's position. If a motor can reach both the MTs at the same time, then there is a 50/50 chance of binding. This means the motor tries to bind to the first MT. If it fails, then it tries to bind to the second MT. In both cases, the binding rate of a motor to a MT is still 2 s^{-1}.
In the course of time, motors can bind and unbind from the MTs as well as switch back and forth between the MTs. The binding, unbinding, and stepping processes of the motors are governed by Micheles-Menten detachment kinetics.

The state of the cargo is defined by the states of the motors. Basically the cargo can be hauled along one or two MTs, depending upon the state of motors. In principle, when the motors can reach both the MTs, this allows the cargo to straddle both MTs when the separation between the MTs is less than twice the native length of the motor.

The run length of the cargo is defined by the total mean distance travelled by the center of mass of the cargo without dissociating from the MT(s). In the simulation, we do not consider the direct motor-motor interactions. However, motors can interact via their forces on the cargo.

3. Effect of Macromolecules Crowding the Cargo

The biological medium differs greatly from an idealized system due to large molecules in the cytoplasm. In particular, in a neuron, owing to the confined geometry of the axon, the effective cargo-protein interactions may be much more pronounced than in an ordinary cell. Axoplasm consists of an abundance of large molecules such as microtubule-associated proteins (MAPs) bound to microtubules (14, 15), the C-termini of neurofilaments medium and heavy with long side arms (15-17), and plectin 1c (18) which is a member of a family of cytoskeletal linking proteins (19).

3.1 Cargo-Protein interaction

3.1.1 Spring-Bead Model

The detail molecular structure and dynamics of the residues of these large molecules using microscopic modeling such as molecular dynamics is computationally challenging and time demanding. In order to get a rough estimate of how a crowded environment affects the cargo dynamics in a confined geometry, we model the cargo-protein interactions by considering each polymer as a chain of spherical beads coupled by massless springs. The motion of each polymer consists of the motion of its constituent beads, each of which diffuses in a constrained environment. In a dense medium, we also incorporate the protein-protein interactions via bead-bead collisions. We assume the interaction is attractive when the beads are far apart and repulsive when they are very close together (at very short range); the interaction is the standard Lennard-Jones (LJ) potential. The LJ potential is useful to model the interaction between particles at the atomic level (20):

$$V_{LJ} = 4\varepsilon\left[\left(\frac{\sigma}{r}\right)^{12} - \left(\frac{\sigma}{r}\right)^{6}\right]$$

The LJ parameters ε and σ are the potential depth and the equilibrium distance of the interparticle separation. r is the distance between the 2 particles. In our simulation, the potential does not enter into the calculation explicitly. We define the forces on the cargo due to polymers, $\boldsymbol{F}_c$, and on the i^{th} bead due to other beads, $\boldsymbol{F}_i$, as the sum of the forces

$$\vec{F}_c = -\sum_{j=1}^{N} \frac{\partial V_{LJ}(c, j)}{\partial r}\hat{r}$$

$$\vec{F}_i = -\sum_{j\neq i}^{N}\left(\frac{\partial V_{LJ}(i, j)}{\partial r}\right)\hat{r} - k_s\left(\vec{x}_{i+1} - \vec{x}_{i-1}\right)$$

where the sum, in principle, runs over all beads, N is the total number of beads, and $\hat{\boldsymbol{r}}$ is a unit vector. The spring constant k_s is defined as

$$k_s = \begin{cases} k & \boldsymbol{x}_{i+1}, \boldsymbol{x}_{i-1} \in \text{same polymer} \\ 0 & \text{otherwise} \end{cases}$$

Each bead and the cargo perform Brownian dynamics with an additional force originating from the interactions, i.e., the positions of the bead and the cargo at any given time are calculated according to

$$\boldsymbol{x}_i(t+\Delta t) = \boldsymbol{x}_i(t) + \frac{\Delta t}{\alpha_T(i)}\boldsymbol{F}_i + \sigma_T(i)\boldsymbol{\varepsilon}_T,$$

$$\boldsymbol{x}_c(t+\Delta t) = \boldsymbol{x}_c(t) + \frac{\Delta t}{\alpha_T(c)}\boldsymbol{F}_c + \sigma_T(c)\boldsymbol{\varepsilon}_T,$$

where the thermal fluctuation coefficients $\sigma_T(i)$ and $\sigma_T(c)$ for the beads and the cargo can be different due to differences in their radii. While the cargo can perform free diffusion, the motion of the beads of each polymer is constrained due to the coupling to the neighboring beads via springs. In order to speed up the simulation, we have also introduced a cut-off in the potential, and the subsequent correction in the derivatives is added into the calculation in order to avoid the divergence in the spatial derivatives that come from the abrupt cut-off. In all our calculations, the cut-off distance is defined in terms of σ, the equilibrium distance of the LJ potential.

The parameter values for the cargo-bead simulations are listed in Table S2.

Table S2: Cargo-Protein Interaction Parameters and Values

Parameters	**Values**	**Comments**
η_0	10 η_w	η_w : viscosity of water
r_b	10 nm	Bead size
σ_b	1.12(2 r_b)	Bead equilibrium distance
σ_c	1.12(a+2 r_b)	Cargo-bead equilibrium distance
ε	1	Potential depth
L_z	1.6 μm	Length of the cylinder
k_s	2 pN/nm	Spring constant

3.1.2 Boundary Condition and Wall Effect

In order to find the mobility and effective viscosity in our simulations, we consider a cylindrical tube of diameter D, and longitudinal dimension L_z, filled with a medium of viscosity η_0. The volume concentration C of the polymers is defined by the ratio

$$C = \frac{V_p}{V_t}$$

where V_p and V_t are the net volume occupied by the polymers and the volume of the tube, respectively. The spherical cargo has radius a. At $t = 0$, we place the cargo at a distance $L_z / 4$ along the axis of the tube and apply an external force F so that it can move in the z-direction. (The cargo is not being hauled along the microtubule by motors; it is being driven by the external force F.) We end the simulation when the cargo reaches the point $3L_z / 4$. We record the time for the net displacement of $L_z / 2$. During this time the cargo as well as polymers can interact with their surroundings and can also experience the resistance from the wall. The wall effect for both cargo and the polymers is incorporated by rescaling the viscosity $\eta \to \eta_{eff} = K(\boldsymbol{x})\eta_0$ during the diffusion process.

3.1.3 Cargo Mobility and effective viscosity

When the cargo interacts with the beads in a polymer, it recoils due to Newton's third law. The recoil velocity of the cargo is much smaller than that of the bead due to a large cargo-bead size ratio. This effect can be significant if the polymer concentration is high.

In order to quantify the effect of the polymer-cargo interactions, we define cargo mobility μ and size-dependent effective viscosity η_{eff} as follows:

$$\mu = \frac{|\boldsymbol{v}|}{|\boldsymbol{F}|},$$

$$\eta_{eff} = \frac{|\boldsymbol{F}|}{6\pi a |\boldsymbol{v}|},$$

where $\boldsymbol{F}$ is the cargo driving force, a is the cargo radius, and $\boldsymbol{v}$ is the average velocity. The effective viscosity can also be found directly by using Stokes' formula:

$$\frac{\eta_{eff}}{\eta_0} = \frac{|\boldsymbol{v}|}{|\boldsymbol{v}_0|}$$

The average velocity in our simulation is calculated by measuring the average time for the cargo to travel through a given distance. We assume that the crowding and confinement renormalize the effective viscosity of the medium. This viscosity changes with the size of the cargo, the length and the density of the polymers, and the strength of the lateral confinement, i.e., the axonal caliber.

4. Results

4.1 Wall effect on transport by a single motor

We first explored how the wall would modify axonal transport of a cargo hauled by a single kinesin motor. We modeled the axon as a long cylinder of uniform diameter with a microtubule centered along the axis of the axon. (In practice, electron micrograph images (21) show a wide variation both in the caliber size and longitudinal undulation.) We investigated the magnitude of the wall effect on cargo motion via our simulations (Fig. S2), and consistent with the analytic results in Fig. 1, observed that the importance of the wall depended very much on the size of the cargo relative to the axon. For a D = 1200 nm axon with η_∞ = 10 times that of water, and with the 500 nm diameter cargo, the average load on the motor during the simulation was approximately 0.84 pN; the effect of such a load in our simulations in the presence of Brownian motion was consistent with past experimental results (11) and previous force-processivity data (11). Thus, for some parameter values, the effect of the increased drag due to the wall effect can be enough to decrease by approximately 50% the expected mean travel distance of a cargo that is hauled by a single motor. Such an effect would likely not be insignificant from a physiological point of view, since recent work (22) suggests that a roughly 25% decrease in motor processivity is enough to have significant consequences. Note that the parameters for the large cargo/small axon case considered are not unreasonable, since mitochondria are frequently on the order of 200 nm in diameter (23), and there are numerous axons on the order of 1 μm in diameter.

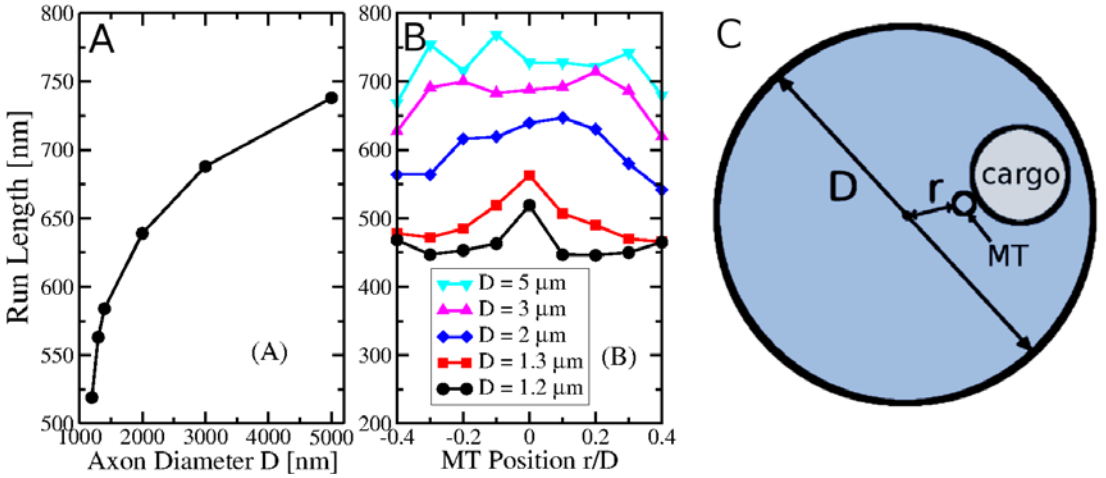

FIGURE S2 (*A*) Run length of a single motor hauling a cargo of radius a = 250 nm as a function of axon diameter when the microtubule (MT) is along the axis of the axon. The expected value of the run length of a cargo in water hauled by a kinesin molecule without any wall is about 800 nm **(24)**. In our simulation, the viscosity of the medium is 10 times that of the water **(7)** and the run length asymptotically approaches the unbounded value when the axon diameter approaches infinity. (*B*) Run length of a cargo hauled by a single motor versus the scaled distance r/D of the microtubule from the axis of the axon for different axon diameters D. r is the distance of the center of the MT from the center of the axon. The MT is parallel to the axis of the axon. The position of the MT with respect to the diameter D of the axon has been rescaled so that all data fits in a single plot. For large axons, the run

lengths fairly remain constant except when the MT is close to the wall. For small caliber axons, the run length increases slightly when the MT is along the axon axis. Here each data point is the average of 1000 runs. (*C*) Cartoon depicting cross section of axon of diameter *D* with MT center a distance *r* from the axon center, and the cargo touching the MT.

4.2 Potential effect of crowding

The biological medium differs from an idealized Newtonian fluid, in part due to large molecules or parts of large molecules that can impede cargo motion due to steric hindrance. To investigate theoretically how large molecules could hinder cargo transport through such effects, we included polymers in our simulations as described in the Methods section.

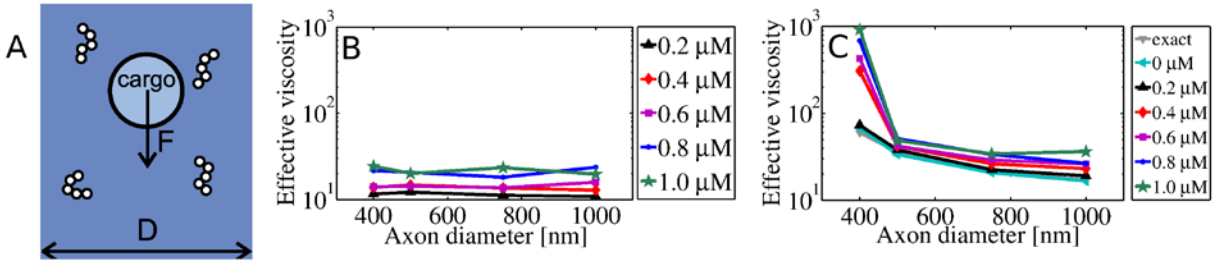

FIGURE S3 (*A*) Cartoon depicting the simulation used to calculate the effective viscosity. A sphere subjected to a constant force *F* moves through a cylinder of diameter *D* containing a fluid with polymers. (*B*) Effective viscosity of the medium in the presence of 200 nm long polymer chains consisting of 10 beads, each with 20 nm diameter as a function of axon diameter D *without* the wall effect (correction factor K=1 in Eq. 2). In the absence of the enhanced viscosity near the wall, the caliber size of the axon does not have any noticeable effect. (*C*) Effective viscosity *with* the wall effect. For comparison, the exact viscosity for a cargo moving along the axis given by Haberman and Sayre (1, 2) is also shown at 0% polymer concentration. Note that the concentration of the polymers enhances the viscosity significantly. This enhancement is very pronounced for small caliber axon when the wall effect is incorporated. Here the radius of the cargo is a = 100 nm and the length of the polymer is set at L = 200 nm. The concentration in μM refers to the number of micromoles of polymer per liter.

Obviously, the higher the polymer concentration, the more effect it had. Thus, we investigated the effect of macromolecules in the axoplasm on the effective viscosity for concentrations of 0, 0.2, 0.4, 0.6, 0.8, and 1.0 μM, corresponding to approximate excluded volumes of 0%, 0.5%, 1%, 1.5%, 2%, and 2.5%. To keep the polymer concentration constant for different caliber axons, we varied the number of polymers as we varied the axon diameter. Each polymer was modeled by a chain containing between 10 beads, each of radius 10 nm coupled through a tiny spring with spring constant 2.0 pN/nm. Because many axonal cargos are small, the cargo radius was fixed at 100 nm, while the diameter of the axon (tube) was varied from 400 nm to 1000 nm. Both the viscosity and mobility data show a clear deviation from the free transport values due to cargo-polymer interactions and the wall effect.

In Fig. S3, we separate the effect of confinement and of crowding by the polymers on the cargo mobility (quantified in terms of effective viscosity) for different polymer concentrations. In Fig. S3*B*, we show the effect of the presence of polymers alone, without incorporating the wall effect on the polymer

filaments and on the cargo. There was a significant enhancement of the "base" viscosity of the medium as the concentration of the polymer increased. This enhancement came from the excluded volume effect. When the wall effect was included (see Fig. S3*C*), the effective viscosity remained fairly constant for a given volume exclusion (polymer concentration) in large diameter axons. However, the wall effect became important and was the dominant factor inhibiting cargo mobility as the caliber size decreased, and the presence of the polymers increased the wall effect. The length scales for which the wall effect became important are discussed next.

4.3 Onset of the wall effect when the cargo radius and cargo-wall distance are comparable

Noting that the presence of long molecules dramatically enhanced the opposition to the motion for even a relatively small cargo in a small caliber axon, we wanted to better understand how the onset of huge resistance depended on the different length scales of the system. The explicit lengths involved in the system were the radius of the cargo (a), the diameter of the axon caliber (D), and the length of the polymers (L), and the distance of the surface of the cargo to the inner wall of the axon (h).

For a Newtonian fluid, the mobility of a spherical object is inversely proportional to its size, while the coefficient of viscosity is the property of the medium, and is size independent. Cytosol, especially the axoplasm, is a complex fluid with large molecules, and is expected to be a non-Newtonian fluid, i.e., the mobility and thus the effective viscosity should vary with the size of the object. In our simulation, as indicated above, we modeled each polymer chain as a system of beads coupled by tiny springs. The size and the number of beads determined the net volume exclusion. We varied the length of the polymer by changing the number of beads linked together while keeping the overall density of the beads (excluded volume) constant. We also varied the size of the cargo as well as the diameter of the axon.

For a small caliber axon, when thermal fluctuations pushed the cargo away from the axonal axis, the average cargo-wall distance, h, could be comparable to the polymer length. In that case one might expect strong cargo-wall coupling via the polymers, leading to a large resistance to cargo transport. However, we observed a very weak dependence on the length of the polymer, as long as the volume exclusion remained constant (see the Supporting Materal), suggesting that such direct cargo-wall coupling via filaments was not a dominant effect.

For a given polymer concentration (volume exclusion), however, the wall effect was significantly amplified by the presence of the polymer when the cargo was relatively close to the wall. In Fig. S3, we see that the wall effect for a given polymer concentration with a small cargo was fairly constant for large caliber axons: its effect was noticable only when the axon diameter was reduced to about D = 400 nm. Here, the cargo radius was 100 nm, so the corresponding ratio of h (distance of cargo surface to the wall) divided by a (cargo radius) was h/a = 1. We investigated whether the observed onset of a dramatic enhancement of the effective viscosity (or the reduction of the mobility) seen in Fig. S3 occurred more generally for cargos of other sizes, at around the same value h/a = 1 (Fig. 2). We observed that it did, for all polymer concentrations and for all polymer lengths; the presence of long molecules increased the 'base' viscosity of the axoplasm, which then resulted in amplifying the magnitude of the wall effect.

To understand whether the ratio h/a was a truly universal quantity, we varied the cargo size for different axon diameters in the regime where $h/a \approx 1$ for a concentration of polymers equal to 4.17% excluded volume. These concentrations were 16.5 μM, 3.31 μM, and 0.827 μM for polymers of lengths 20 nm,

100 nm, and 400 nm, with beads of radius 10 nm. In Fig. 2, we show the extracted effective viscosity data for different calibers and cargo radii expressed in terms of the parameter h/a. It is interesting to note that, irrespective of the axon or cargo size, the effective viscosity dramatically increased when $h/a \leq 1$ for all axon and cargo dimensions. Physically, small h meant that the cargo was close to the wall, and large a meant that there was a large amount of cargo surface area to enhance the viscous drag produced by proximity to the wall of the axon. Thus the wall effect became insignificant if the cargo-axon geometry satisfied the condition $h/a \gg 1$.

5. Relation between the load on the motor and the location of the microtubule

The cargo is subjected to a greatly enhanced viscosity when it is very close to the wall of the axon. For this reason, it avoids the wall. Suppose the cargo is close to the wall of the axon. As the motor walks along the MT and pulls on the cargo, the wall exerts a drag force parallel to the wall and the MT. This force stretches the motor. The component of the force perpendicular to the wall and the MT pushes the cargo down toward the MT. In our simulations we find that the cargo avoids being close to the wall. In Figure S4*A*, we plot the run length vs. load on the motor at the time when the motor detaches from the MT for a large and small diameter axon. The load on the motor is given by the amount that the motor is stretched multiplied by the spring constant of the motor. For small loads, the average run length (travel distance) is about the same for both axon sizes. However, for large loads (greater than 8 pN), the run length is considerably shorter for the smaller caliber axon. Figures S4*B* and S4*C* show that the large loads on the motor occur when the cargo is near the microtubule and far from the axon wall. The reduced run length in the small caliber axon is due to the viscosity that is enhanced by the small diameter of the axon. The nominal viscosity of the axoplasm in our simulations is 10 times that of water. With the correction factor (Figure 1 in main paper) of 5 far from the wall, the effective viscosity is about 50 times that of water.

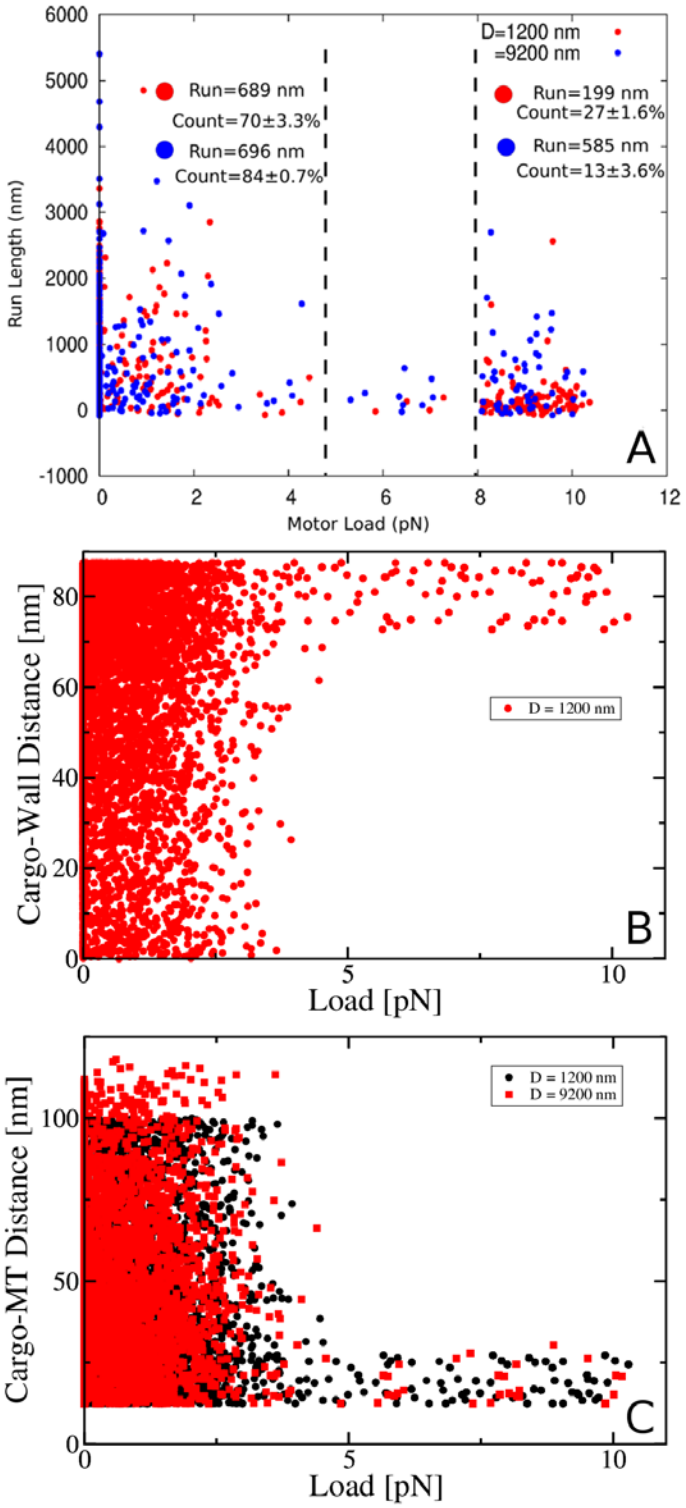

Figure S4: In all of these scatter plots, a single motor hauls a spherical cargo with a radius of 250 nm along a single microtubule centered on the axis of the axon. We show two axon diameters: 1200 nm and 9200 nm. Each point represents a single run. (*A*) Run length versus the load on the motor at the time when the motor detached from the microtubule. The run length is shorter for high loads (> 8 pN) in the

smaller axon. Data is from 400 runs. (*B*) The distance between the inner wall of the axon and the surface of the cargo versus the load on the motor when it detached. (*C*) The distance between surface of the cargo and the surface of the microtubule versus the load on the motor when it detached. Notice that the motor can have a large load when it is near the microtubule, but never when it is near the wall and hence far from the microtubule.

6. Electron Micrograph Images of Axons and Their Microtubule Distribution

Here we present some examples of electron micrograph (EM) images of small caliber axons where we have measured the distribution of microtubules. Electron micrograph images of axonal cross section of small and large motor neurons of mice were analyzed by paying particular attention to the microtubule distributions. In some EMs, the resolution or magnification were such that it was hard to identify microtubules, so those images with indistinguishable microtubules were discarded. To determine whether the microtubules were randomly distributed or not, we overlaid a grid onto the images such that there was an average of roughly one microtubule per grid square. We then counted the number of visible microtubules in each square that was fully contained within the axon's boundary (25). The grid size was such that there was approximately one MT per square, i.e., the side of a grid square ranged from 0.2 to 1 μm. An example is shown in Figure S5. Given the mean number of microtubules per square, we could then use the Poisson distribution with that mean to calculate the probability of finding a given number of microtubules in a square. Values of chi-squared (representing the deviation of the results from the Poisson distribution) and *p* (the probability that the microtubules were randomly distributed) were then calculated. In most cases we found that the MTs were randomly distributed and agreed well with a Poisson distribution (Fig. S5*C*). Of the nine images with readily visible microtubules, eight had p-values greater than 0.05, suggesting microtubules were largely randomly distributed (Figure S5). In some axons the MTs appear to be clustered (see Figure S6) and we find the MTs in a cluster tend to be within 100 nm of each other as long as the overall MT density is comparable to that of similar caliber axons. Figure S6 had a *p*-value below 0.05, suggesting a nonrandom clustering of microtubules. Of course, one axon is not enough to draw any conclusions about whether the microtubule arrangement is random or not; this one axon could simply be one of the rare axons whose arrangement of microtubules puts it in the tail of the Poisson distribution. However, previous work has also found microtubule bundling in axons (16, 26, 27). A summary of the axonal EMs that we examined is shown in Figure S7 where we plot the p-value vs. the MT density of the axon in Figure S7*A* and the *p*-value vs. the cross sectional area of the axon in Figure S7B. The *p*-value represents the probability that the distribution of MTs followed a Poisson distribution. Since a small *p*-value corresponds to a non-random distribution of MTs, we can see that most of the axons had a large *p*-value and thus, a Poisson distribution of MTs, regardless of the axon size, i.e., the axonal cross sectional area.

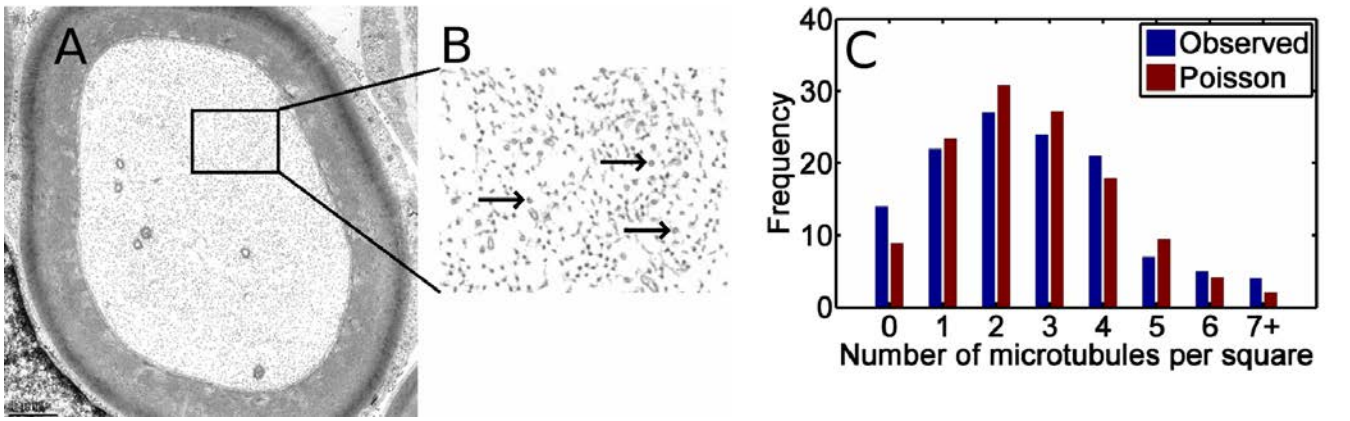

Figure S5. (*A*) Electron Micrograph (EM) image of the cross section of a myelinated axon of a large motor neuron of a 6-month-old mouse. The average inner diameter (excluding myelin) is about 6 microns. The MT density is 28.3 MTs/μm^2. (*B*) A zoomed portion of the cross section. Three arrows point out microtubules. Other microtubules are clearly visible. (*C*) Histogram comparing the observed distribution microtubules with the Poisson distribution (Poisson mean = 2.6371 MT/square). Good agreement with the Poisson distribution indicates that the MTs are randomly distributed. The *p*-value for a Poisson distribution of MTs is 0.5 in this case. The EM was analyzed by overlaying a square grid on the axon and counting the number of microtubules in each square. The mesh size was such that there was approximately 1 MT per grid square.

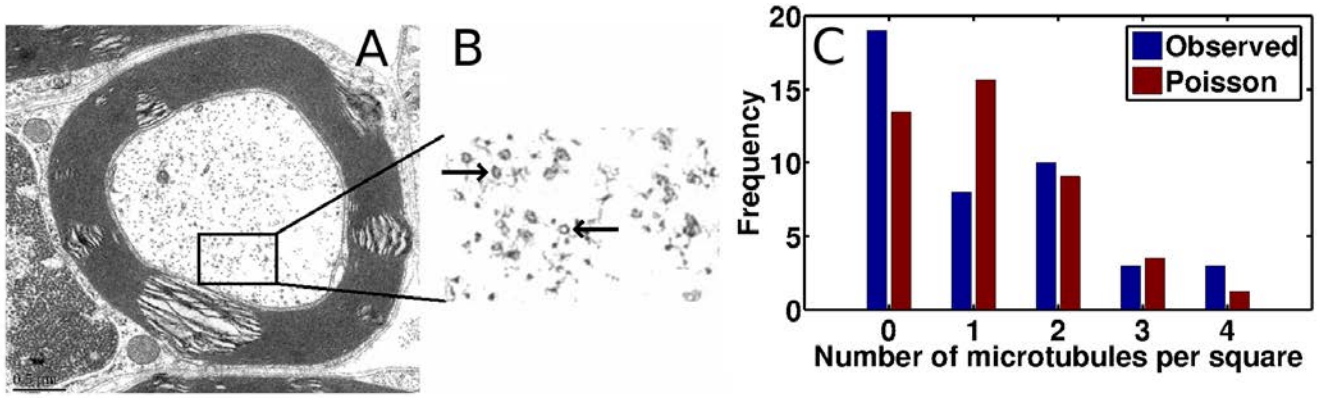

Figure S6. (*A*) Electron Micrograph (EM) image of the cross section of a myelinated axon of a small motor neuron of a 6-month old mouse. The average inner diameter (excluding myelin) is about 2.08 micron. The MT density is 3.2 MTs/μm^2. (*B*) A zoomed portion of the cross section. Two arrows point out microtubules. Other microtubules are clearly visible. (*C*) Histogram comparing the observed distribution microtubules with the Poisson distribution (Poisson mean = 0.9143 MT/square). Analysis was the same as in Figure S5. Poor fit to Poisson distribution indicates that the MTs were clustered. The *p*-value for a Poisson distribution of MTs is 0.035 in this case. However, since this is just one axon, one cannot draw any definite conclusions about whether the microtubule arrangement is random or not; this axon could simply be one of the rare axons whose arrangement of microtubules occurs 3.5% of the time in a Poisson distribution.

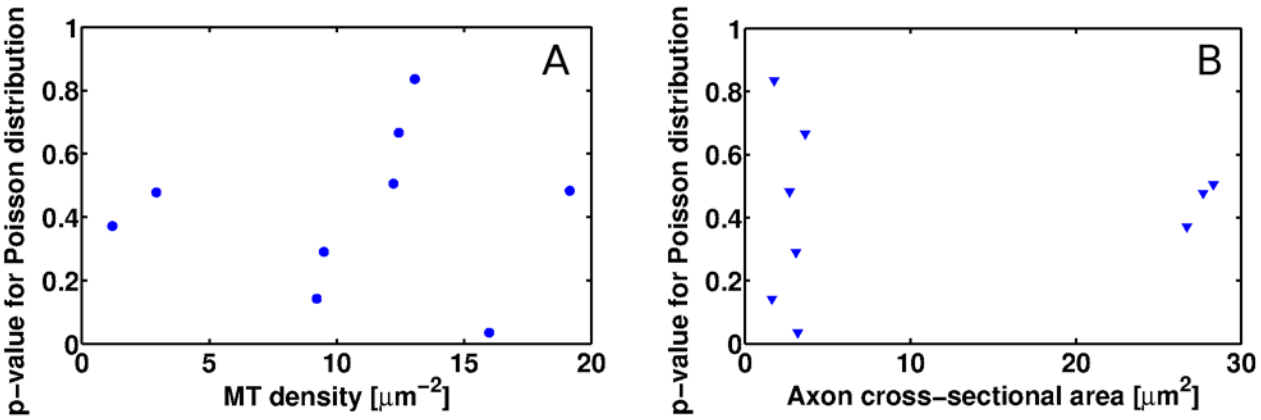

Figure S7. (*A*) *P*-value of Poisson distribution of microtubules versus the MT density. Each point represents the MTs in one axon. Low *p*-value indicates that the MTs are clustered and not randomly distributed. High *p*-value means that the MTs are distributed randomly according to a Poisson distribution. (B) *P*-value of Poisson distribution versus the cross-sectional area of the axon. Note that most of the axons have a random distribution of MTs, regardless of their size (cross-sectional area).

If the microtubules are randomly distributed, we can calculate likely nearest-neighbor distances given the average microtubule density. Given an average MT density ρ, the probability P that some MT will have a nearest neighbor within a distance r is (28):

$$P = 1 - e^{-\rho\pi r^2}$$

(Note that this expression goes to zero as r goes to zero, and to 1 as r goes to infinity; it increases with ρ.) Solve for ρ:

$$\rho = \frac{-\ln(1-P)}{\pi r^2}$$

We plot this equation in Figure 5 in the main text. A center-to-center distance of 75 nm between adjacent microtubules is more than sufficient for a single motor within range of the MTs to reach either of them, as discussed in the main text. If we set r to 75 nm, we can calculate values of ρ for different desired values of P as shown in Table S3.

Table S3: Microtubule Densities Needed For Various Nearest-Neighbor Probabilities at 75 and 200 nm

P (neighbor within distance)	ρ (MTs / μm^2), 75 nm	ρ (MTs / μm^2), 200 nm
0.75	78.45	11.03
0.8	91.08	12.81
0.9	130.3	18.32
0.95	169.5	23.84
0.99	260.6	36.65

Smaller-caliber axons have recorded microtubule densities of roughly 150 microtubules/μm^2, meaning a microtubule has a greater than 90% chance of having a neighbor within 75 nm. As mentioned above, some axons do appear to exhibit clustering in microtubules rather than random distribution; in these cases, the closest neighbors in a cluster are well within 75 nm.

For contrast, we also include the microtubule densities necessary for a microtubule to have a neighbor within 200 nm, although a separation this great makes multiple-microtubule transport unlikely. In the images of larger axons with the most clearly visible microtubules, microtubule densities ranged from roughly 12-25 microtubules/μm^2, corresponding to at least a 75% chance of any given microtubule having a neighbor within 200 nm.

7. More realistic modeling of axonal transport

The purpose of this paper has been to point out that there can be significant viscous drag on cargos moving close to the axonal wall, which effectively acts as a rigid wall. We have used a simple model of axonal transport to illustrate this, but there are clearly ways in which the model of axonal transport could be made more realistic. For example, we have modeled the cargo as a rigid sphere, but a variety of cargos with different shapes undergo fast axonal transport, e.g., membranous organelles and tubules, mitochondria, vesicles containing neurotransmitters, lysosomes, etc. (29). Some of these cargos could be deformed as they pass near the axon wall or near other cargos. In addition, we have modeled axoplasm as an isotropic viscous fluid containing polymers, even though it is a complex anisotropic heterogeneous viscoelastic fluid (30) containing polymers, and membranous organelles and tubules largely oriented along the axis of the axon. One way to model the axoplasm would be with the Burger's model which involves elastic moduli and viscous coefficients a circuit-type arrangement (30). In addition to the viscosity enhancement near the wall of the axon, the membranous tubules, e.g., the endoplasmic reticulum, in the axoplasm could also enhance the viscosity experienced by nearby cargos. This enhancement is not seen in nonneuronal cells as found in experiments where a reduction in the number of motors hauling lipid droplet in *Drosophila* embryos did not reduce the run length or the velocities of the cargo (13). Thus, it appears that at least without a nearby bounding membrane, intracellular membranes do not impair intracellular transport in nonneuronal cells because the vesicles are able to avoid close approaches where the viscosity is greatly enhanced. However, avoiding such close

encounters is not always possible in the confined geometry of the axon. This would explain why, as we mentioned above, inhibition of force generation by dynein arrested the motion of large lysosomes/late endosomes in axonal transport but had little effect on the transport of small vesicles (22). To model transport in the axon in the presence of membranous tubules is difficult because it requires too many unconstrained parameters such as the tubules' size, shape, location, and whether they are tethered or free floating. However, we believe that cargo transport via motors walking along two MTs simultaneously could be especially helpful in small caliber axons where pushing such membranous tubules out of the way is difficult because of the confined geometry. In addition, interactions between cargos traveling in opposite directions could also impair cargo transport, e.g., the organelle traffic jams (31, 32) that we mentioned above, but modeling this is well beyond the scope of this paper which just considers single cargo transport. Although our modeling suggests that small cargos like synaptic vesicles (~100 nm) can be transported in an axon without significant resistance, other larger cargos like mitochondria and lysosomes (22) may have more difficulties, especially in small caliber axons. This work thus provides a useful conceptual framework for such effects but the extent to which such scenarios contribute to disease progression in the animal remains to be explored experimentally.

SUPPORTING REFERENCES

1. Happel, J., and H. Brenner. 1965. Low Reynolds Number Hydrodynamics, With Special Applications to Particulate Media. Prentice-Hall, Englewood Cliffs, NJ.
2. Haberman, W. L., and R. M. Sayre. 1958. Motion of rigid and fluid spheres in stationary and moving liquids inside cylindrical tubes. In David Taylor Model Basin Report (no. 1143). Department of the United States Navy.
3. Brenner, H., and J. Happel. 1958. Slow viscous flow past a sphere in a cylindrical tube. *J Fluid Mech* 4:195-213.
4. Bungay, P. M., and H. Brenner. 1973. The Motion of a Closely-Fitting Sphere in a Fluid-Filled Tube. *International Journal of Multiphase Flow* 1:25-56.
5. Tozeren, H. 1982. Torque on eccentric spheres flowing in tubes. *J Appl Mech-T Asme* 49:279-283.
6. Ambari, A., B. Gauthier-Manuel, and E. Guyon. 1984. Wall effects on a sphere translating at constant velocity. *J Fluid Mech* 149:235-253.
7. Haak, R. A., F. W. Kleinhans, and S. Ochs. 1976. The viscosity of mammalian nerve axoplasm measured by electron spin resonance. *J. Physiol.* 263:115-137.
8. Greenstein, T., and J. Happel. 1968. Theoretical study of the slow motion of a sphere and a fluid in a cylindrical tube. *J Fluid Mech* 34:705-710.
9. Erickson, R. P., Z. Jia, S. P. Gross, and C. C. Yu. 2011. How molecular motors are arranged on a cargo is important for vesicular transport. *PLoS Comput. Biol.* 7:e1002032.
10. Visscher, K., M. J. Schnitzer, and S. M. Block. 1999. Single kinesin molecules studied with a molecular force clamp. *Nature* 400:184-189.
11. Kunwar, A., M. Vershinin, J. Xu, and S. P. Gross. 2008. Stepping, strain gating, and an unexpected force-velocity curve for multiple-motor-based transport. *Curr. Biol.* 18:1173-1183.
12. Block, S. M., L. S. Goldstein, and B. J. Schnapp. 1990. Bead movement by single kinesin molecules studied with optical tweezers. *Nature* 348:348-352.
13. Shubeita, G. T., S. L. Tran, J. Xu, M. Vershinin, S. Cermelli, S. L. Cotton, M. A. Welte, and S. P. Gross. 2008. Consequences of motor copy number on the intracellular transport of kinesin-1-driven lipid droplets. *Cell* 135:1098-1107.

14. Voter, W. A., and H. P. Erickson. 1982. Electron microscopy of MAP 2 (microtubule-associated protein 2). *J. Ultrastruct. Res.* 80:374-382.
15. Mukhopadhyay, R., S. Kumar, and J. H. Hoh. 2004. Molecular mechanisms for organizing the neuronal cytoskeleton. *BioEssays : news and reviews in molecular, cellular and developmental biology* 26:1017-1025.
16. Hirokawa, N. 1982. Cross-linker system between neurofilaments, microtubules, and membranous organelles in frog axons revealed by the quick-freeze, deep-etching method. *J. Cell Biol.* 94:129-142.
17. Hirokawa, N., S. Hisanaga, and Y. Shiomura. 1988. MAP2 is a component of crossbridges between microtubules and neurofilaments in the neuronal cytoskeleton: quick-freeze, deep-etch immunoelectron microscopy and reconstitution studies. *J. Neurosci.* 8:2769-2779.
18. Fuchs, P., M. Zorer, S. Reipert, G. A. Rezniczek, F. Propst, G. Walko, I. Fischer, J. Bauer, M. W. Leschnik, B. Luscher, J. G. Thalhammer, H. Lassmann, and G. Wiche. 2009. Targeted inactivation of a developmentally regulated neural plectin isoform (plectin 1c) in mice leads to reduced motor nerve conduction velocity. *J. Biol. Chem.* 284:26502-26509.
19. Wiche, G., and L. Winter. 2011. Plectin isoforms as organizers of intermediate filament cytoarchitecture. *Bioarchitecture* 1:14-20.
20. Hansen, J.-P., and I. R. McDonald. 1990. Theory of Simple Liquids. Academic Press, London.
21. Tang-Schomer, M. D., A. R. Patel, P. W. Baas, and D. H. Smith. 2010. Mechanical breaking of microtubules in axons during dynamic stretch injury underlies delayed elasticity, microtubule disassembly, and axon degeneration. *FASEB J.* 24:1401-1410.
22. Yi, J. Y., K. M. Ori-McKenney, R. J. McKenney, M. Vershinin, S. P. Gross, and R. B. Vallee. 2011. High-resolution imaging reveals indirect coordination of opposite motors and a role for LIS1 in high-load axonal transport. *J. Cell Biol.* 195:193-201.
23. Kaasik, A., D. Safiulina, A. Zharkovsky, and V. Veksler. 2007. Regulation of mitochondrial matrix volume. *Am. J. Physiol. - Cell Ph.* 292:C157-163.
24. Schnitzer, M. J., K. Visscher, and S. M. Block. 2000. Force production by single kinesin motors. *Nat. Cell Biol.* 2:718-723.
25. Zar, J. H. 1974. Biostatistical Analysis. Prentice-Hall, Englewood Cliffs, NJ.
26. Yamada, K. M., B. S. Spooner, and N. K. Wessells. 1971. Ultrastructure and function of growth cones and axons of cultured nerve cells. *J. Cell Biol.* 49:614-635.
27. Friede, R. L., and T. Samorajski. 1970. Axon caliber related to neurofilaments and microtubules in sciatic nerve fibers of rats and mice. *Anat. Rec.* 167:379-387.
28. Zwillinger, D. 2003. CRC Standard Mathematical Tables and Formulae. CRC Press, Boca Raton.
29. Perrot, R., and J. P. Julien. 2009. Real-time imaging reveals defects of fast axonal transport induced by disorganization of intermediate filaments. *FASEB J.* 23:3213-3225.
30. Sato, M., T. Z. Wong, D. T. Brown, and R. D. Allen. 1984. Rheological properties of living cytoplasm: a preliminary investigation of squid axoplasm *(Loligo pealei). Cell Motil.* 4:7-23.
31. Hurd, D. D., and W. M. Saxton. 1996. Kinesin mutations cause motor neuron disease phenotypes by disrupting fast axonal transport in *Drosophila*. *Genetics* 144:1075-1085.
32. Gindhart, J. G., Jr., C. J. Desai, S. Beushausen, K. Zinn, and L. S. Goldstein. 1998. Kinesin light chains are essential for axonal transport in *Drosophila*. *J. Cell Biol.* 141:443-454.